View metadata, citation and similar papers at core.ac.uk

brought to you by CORE

provided by Elsevier - Publisher Connector

Progress in Natural Science: Materials International 2012;22(6):592–615

Chinese Materials Research Society

Progress in Natural Science: Materials International

www.elsevier.com/locate/pnsmi
www.sciencedirect.com

REVIEW

ABO_3-based photocatalysts for water splitting

Jinwen Shi, Liejin Guo*

International Research Center for Renewable Energy, State Key Laboratory of Multiphase Flow in Power Engineering (MFPE), Xi'an Jiaotong University (XJTU), 28 West Xianning Road, Xi'an, Shaanxi 710049, China

Received 22 July 2012; accepted 8 November 2012
Available online 18 January 2013

KEYWORDS

Perovskite;
Band structures;
Micro-/nano-structures;
Local lattice structures;
Energy conversion;
Photochemistry

Abstract ABO_3-based photocatalysts for water splitting were systematically reviewed in this manuscript. Crystal structure and chemical composition characteristics of ABO_3 materials were briefly introduced to guide the modification of ABO_3-based photocatalysts. The ABO_3-based photocatalysts were then reviewed in detail and divided into four groups based on the employed modification strategies, i.e., chemical component adjustment, micro-/nano-structure adjustment, local lattice structure adjustment, and application of the modification strategy of ABO_3 photocatalysts in designing $A_xB_yO_z$ photocatalysts. In this section, the recent research works on ABO_3-based photocatalysts in our group were presented. Finally, application of ABO_3 photocatalysts in *Z*-scheme systems for overall water splitting was introduced. This review summarized the development of ABO_3-based photocatalysts and showed the values and possible direction of future research, thereby offering a guide for photocatalytic water splitting.

© 2013 Chinese Materials Research Society. Production and hosting by Elsevier B.V. All rights reserved.

1. Introduction

Energy shortage and environmental pollution have become two urgent problems that restrict social development and endanger human survival. In order to resolve the two issues and to realize the sustainable development of society, the most effective route is the active development and utilization of clean and renewable energy sources, among which solar energy is the most promising candidate due to its abundant reservation and wide distribution. However, the large scale utilization of solar energy is still restricted at present due to its low energy density, high geographical dispersion, high time instability, and inconvenience for storage. H_2 is a kind of superior energy carrier and ideal clean and renewable energy due to its high energy density, no pollution from the combustion products, convenience for storage and transportation. Consequently, exploring and realizing the conversion and storage of solar energy as hydrogen energy is a powerful route to develop and utilize renewable energy [1]. Photocatalytic H_2 evolution under solar light irradiation has shown good prospect for such a conversion, and photocatalytic overall water splitting to form both H_2 and O_2 stoichiometrically under solar light irradiation is the ultimate goal to realize such a conversion by

*Corresponding author. Tel.: +86 29 8266 0996; fax: +86 29 8266 9033.
E-mail address: lj-guo@mail.xjtu.edu.cn (L. Guo).

Peer review under responsibility of Chinese Materials Research Society.

ELSEVIER Production and hosting by Elsevier

1002-0071 © 2013 Chinese Materials Research Society. Production and hosting by Elsevier B.V. All rights reserved.
http://dx.doi.org/10.1016/j.pnsc.2012.12.002

photocatalysis [2]. Furthermore, in order to develop the system for photocatalytic overall water splitting under solar light irradiation, it is a key task to exploit photocatalysts with high stability, high efficiency, low cost for visible-light-driven H_2 and O_2 evolution.

The developed photocatalytic materials for H_2 and O_2 evolution mainly contain inorganic semiconductors [3–7], metal organic complexes [8–10], organic semiconductors [11,12], and recently reported conductors [13], in which inorganic semiconductor photocatalysts showed great promising for future applications [14–17].

2. Semiconductor photocatalysis for water splitting

The fundamental principle and processes for semiconductor-based photocatalytic water splitting have been clearly presented in many excellent review papers [14–16,18–28] and raised the basic requirement for water-splitting photocatalysts as follows to guide the exploration of such photocatalytic materials.

Considering the fundamental principle, photocatalyst should have bandgap larger than the standard Gibbs free energy change (1.23 eV) for water splitting into H_2 and O_2, and should have conduction band with potential more negative than that for water reduction and valence band with potential more positive than that for water oxidation. Furthermore, based on the processes, firstly, photocatalyst should have bandgap smaller than the energies of incident photons to ensure the excitation of photogenerated charge carriers. Visible light accounts for around 43% of the incoming solar energy, and therefore should be fully used by photocatalysts with excellent visible-light response. Secondly, photocatalyst should have good ability to promote the separation and transfer of photogenerated charge carriers and thus to restrain their recombination. Thirdly, photocatalyst should provide enough reactive sites to accelerate redox reaction and to restrain the back-reaction. In a word, in order to improve the photocatalytic reaction, photocatalyst should enhance the generation, transfer, and reaction of photogenerated charge carriers during the whole photocatalytic process.

According to the types of anions, inorganic semiconductor photocatalysts were mainly classified as S-containing, N-containing, and oxide photocatalysts. In contrast, oxide photocatalysts generally showed unparalleled stability that is the most basic and important requirement of photocatalysts for practical application, and therefore are of great research value. However, the ability of oxide photocatalysts to utilize visible light was often intrinsically restrained by the wide bandgaps, which were usually caused by the low valence bands that consisted of O 2p orbitals with a potential of around 3.0 eV versus NHE [20]. Moreover, the activities of developed visible-light-driven oxide photocatalysts were still low [3]. Accordingly, the research focus on oxide photocatalysts should be the extension of light-response ranges and the enhancement of visible-light-driven photocatalytic activities [29].

In this review paper, we focus on ABO_3-based photocatalysts in view of the following characteristics of ABO_3 materials.

3. Characteristics of ABO_3 materials

3.1. *Crystal structure characteristics of ABO_3 materials*

ABO_3 represents a class of typical binary metal oxides. A series of ABO_3 with crystal structures could be obtained by using different elements and preparation conditions. By taking the prevalent perovskite ABO_3 as an example, the crystal structure characteristics were introduced as follows so as to indicate the advantages and prospects of ABO_3 materials for the application to photocatalytic water splitting under solar irradiation.

ABO_3 with ideal cubic perovskite structure (space group, $Pm\bar{3}m$) is shown in Fig. 1. Metal cations in A and B sites are located in the 12- and 6-coordinated environments with O anions, respectively, and the radii of A-site cations are generally larger than those of B-site cations. Eight BO_6 octahedra with shared corners formed the three-dimensional framework of cubic cell, the center of which is occupied by A-site cation. The radii of cations varied due to different types and valence states of cations. Consequently, compared with the ideal cubic perovskite ABO_3, the real perovskite ABO_3 exhibited lattice distortion to varying degrees, thereby resulting in the transformation of crystal phases in the following sequences: orthogonal, rhombohedral, tetragonal, monoclinic, and triclinic phase. As far as photocatalysis is concerned, lattice distortion has important impact on crystal field and thus changes the dipole and electronic band structures, thereby influencing the behaviors of photogenerated charge carriers, including excitation, transfer, and redox reaction, in whole photocatalytic process [30–32].

3.2. *Chemical composition characteristics of ABO_3 materials*

Most metal elements in periodic table are known to be stably located in ABO_3 structures, and multicomponent ABO_3 materials can be easily synthesized by partial substitution of cations in A and B sites. In terms of photocatalysts, control of electronic band structures by adjusting elemental compositions was accepted as the effective method to extend light-response range. For this reason, ABO_3 structures provide the basic framework and extensive space for the combination of elemental compositions and the construction of electronic band structures in photocatalysts [33–38].

Moreover, owing to the requirement of charge balance for in A and B sites, the mixed oxidation states or unusual

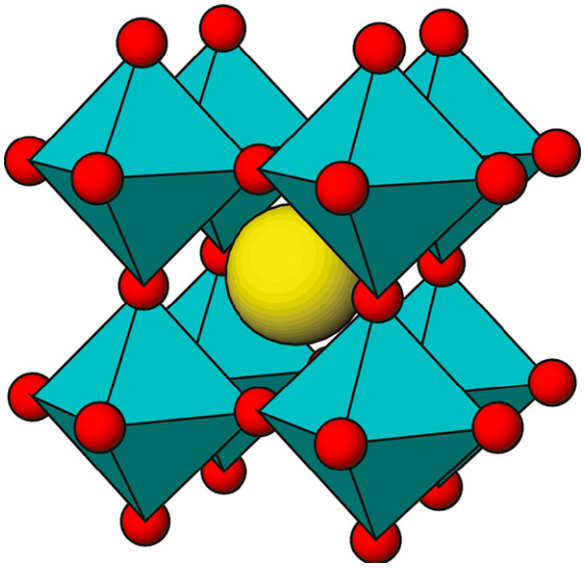

Fig. 1 Ideal cubic perovskite structure for ABO_3 (cyan, BO_6 units; yellow, A atoms). Reprinted with permission from Ref. [27].

oxidation states of metal cations were expected to be maintained in ABO_3 structures. With regard to photocatalysts, valence states of elements generally play key roles in determining the ability of light response and the lifetime of photogenerated charge carriers. Accordingly, ABO_3 structures can be employed to guarantee the valence-state control of metal cations in photocatalysts [39,40].

Besides, the easy preparation and controllable physicochemical properties make ABO_3 materials excellent model photocatalysts for the investigation of structure–activity relationships during photocatalytic reaction.

4. Development of ABO_3 photocatalysts

Based on the crystal structure and chemical component characteristics, different modification strategies (such as chemical component adjustment, micro-/nano-structure adjustment, and local lattice structure adjustment) were employed to develop ABO_3 photocatalysts with improved performance for water splitting (see Table 1).

4.1. *Chemical component adjustment*

The approaches to chemical component adjustment of ABO_3 photocatalysts are mainly divided into ion doping, ion replacement, multi-component solid solution, multi-component composite.

4.1.1. *Ion doping*

Ion doping includes interstitial doping and lattice substitution. Ions are generally doped into ABO_3 materials by means of lattice substitution. ABO_3 (such as $SrTiO_3$ [81,122–128] and $NaTaO_3$ [50]) showed unparalleled stability and high activity for photocatalytic H_2 and/or O_2 evolution especially for overall water splitting under ultraviolet (UV) irradiation [50,81,122–128], but the ability to utilize visible light was often intrinsically restrained by wide bandgaps [20]. Accordingly, metal cations were usually doped into ABO_3 (such as $SrTiO_3$ [39,49,55,56,58,73,102] and $NaTaO_3$ [120]) to tailor the electronic structures and thus to extend the light response range [20].

Konta et al. found that Ru-, Rh-, and Ir-doped $SrTiO_3$ possessed intense absorption bands in the visible light region due to excitation from the discontinuous levels formed by the dopants to the conduction band of the $SrTiO_3$ host. Mn- and Ru-doped $SrTiO_3$ showed photocatalytic activities for O_2 evolution from an aqueous silver nitrate solution while Ru-, Rh-, and Ir-doped $SrTiO_3$ loaded with Pt cocatalysts produced H_2 from an aqueous methanol solution under visible light irradiation. Pt/Rh-doped $SrTiO_3$ photocatalyst gave an AQY of 5.2% at 420 nm for the H_2 evolution reaction, and the reducible Rh species contributed to the formation of visible light absorption band and the surface reaction sites [55]. Bae et al. investigated noble metal (Ru, Rh, Ir, Pt, and Pd)-doped $SrTiO_3$ as well, and ascribed the photocatalytic activity of Pt/Rh-doped $SrTiO_3$ to its suitable band energetics, and the induced hybridized Ti/Rh orbitals in the bandgap of $SrTiO_3$ [73]. Chen et al. developed copper doped ABO_3 ($CaTiO_3$ [90] and $LaNiO_3$ [91,94]) photocatalysts for visible-light-driven H_2 evolution and attributed the enhancement of photocatalytic activity to the smaller bandgap and the lowered probability for recombination of electron–hole pairs.

Furthermore, in order to control the valence states of doped metal cations and to reduce the lattice defects in ABO_3 photocatalysts, the strategy of codoping was generally adopted to maintain the charge balance. Kudo et al. developed a series of codoped $SrTiO_3$ photocatalysts, such as (Cr,Sb)-codoped $SrTiO_3$ [49], (Cr,Ta)-codoped $SrTiO_3$ [56], and (Ni,Ta)-codoped $SrTiO_3$ [58], and applied to visible-light-driven photocatalytic H_2 evolution in methanol solution. (Cr,Sb)-codoped $SrTiO_3$ showed intense absorption bands in the visible light region and possessed 2.4 eV of energy gaps, respectively. The charge balance was kept by codoping of Sb^{5+} and Cr^{3+} ions, resulting in the suppression of formation of Cr^{6+} ions and oxygen defects in the lattice which should work as effectively nonradiative recombination centers between photogenerated electrons and holes [49]. Compared with Cr-doped $SrTiO_3$, (Cr,Ta)-codoped $SrTiO_3$ had a shorter induction period and showed higher photocatalytic activity. Codoping of tantalum ions suppressed the formation of Cr^{6+} ions and oxygen defects which would work as nonradiative recombination centers between photogenerated electrons and holes, resulting in the shortening of induction periods and the improvement of photocatalytic activities [56]. As for (Ni,Ta)-codoped $SrTiO_3$, the visible-light responses were due to the charge-transfer transition from the electron donor levels formed by the 3d orbitals of doped Ni^{2+} to the conduction bands of the host materials. (Ni,Ta)-codoped $SrTiO_3$ showed higher activity than $SrTiO_3$ doped with only nickel, because codoped Ta^{5+} ions suppressed the formation of Ni^{3+} ions that are expected to trap photogenerated electrons [58].

In addition, ion doping could be employed not only to extend the light response but also to enhance the photocatalytic activity. Ishihara et al. found for the first time that controlling the charge density in oxide semiconductors with an acceptor was effective for improving the activity for overall water splitting. Although the photodecomposition activity of $NiO/KTaO_3$ was negligible, doping small amount of acceptor (Zr^{4+}) to form NiO/Zr-doped $KTaO_3$ increased the formation rate of H_2 and O_2 [42]. Furthermore, Takata et al. examined the doping of aliovalent metal cations to $SrTiO_3$ photocatalyst for overall water splitting. It was found that doping of a cation (Na^+) with valence lower than that of the parent cation (Sr^{2+}) effectively enhanced photocatalytic activity but the doping of a cation (Ta^{5+}) with valence higher than that of the parent cation (Ti^{4+}) suppressed photocatalytic activity, because the doping of a lower valence cation introduced oxygen vacancies and decreased Ti^{3+}. The concept of defect engineering by aliovalent doping provides an example of the design of active photocatalysts [81].

Based on the above results, it could be found that both the types and valence states of doped transition metals play important roles in enabling the visible-light response and improving the photocatalytic activities, and ABO_3 hosts provide excellent platforms for the modification of ion doping. The basic requirement of charge balance in ABO_3 hosts could be flexibly utilized to intentionally control the valence states of doped transition metals and the lattice defects, thereby optimizing the photocatalytic reaction.

4.1.2. *Ion replacement*

Kato et al. developed $AgMO_3$ (M = Ta and Nb) photocatalysts by replacing Na^+ in $NaMO_3$ (M = Ta and Nb) with Ag^+.

Table 1 ABO_3-based photocatalysts for water splitting.

Photocatalyst (mass)	Preparation strategy	Lamp (filter)[a]	Reactant solution[b]	Activity/ $\mu mol\ h^{-1}\ g_{cat}^{-1}$[c]		AQY/% (wavelength/nm)[d]	Reference (year)
				Cocatalyst/H_2	Cocatalyst/O_2		
$Ga_{2-x}In_xO_3$	Solid-state reaction	450 W Hg	5.4 vol% CH_3OH/0.05 M $AgNO_3$	1 wt% Pt/30[f]	—/25[f]	–	[41] (1998)
Zr-doped $KTaO_3$ (0.1)[e]	Solid-state reaction	500 W Xe	Pure water	1.5 wt% NiO/ 122.3	1.5 wt% NiO/57.4	–	[42] (1999)
La-doped $NaTaO_3$ (1)[e]	Solid-state reaction	400 W Hg	1 mM NaOH	0.2 wt% NiO/ 15000[f]	Stoichiometric ratio	~50 (270)	[43] (2000)
$NaSbO_3$ (0.25)[e]	Solid-state reaction	200 W Hg–Xe	Pure water	1 wt% RuO_2/~6[f]	1 wt% RuO_2/~2[f]	–	[44,45] (2001, 2002)
$NaTaO_3$ (1)[e]	Solid-state reaction	400 W Hg	0.1 mM NaOH (pH = = 10.5)	0.05 wt% NiO/ 3390	0.05 wt% NiO/ 1580	20 (270)	[46] (2001)
$LiTaO_3$ (1)[e]	Solid-state reaction	400 W Hg	Pure water	—/430	—/220	–	[46] (2001)
$KTaO_3$ (1)[e]	Solid-state reaction	400 W Hg	Pure water	—/29	—/13	–	[46] (2001)
$NaTaO_3$ (1)	Solid-state reaction	450 W Hg	0.1 M KNO_3	1 wt% Ni/300	1 wt% Ni/480	–	[47] (2002)
$AgTaO_3$ (0.15)[e]	Solid-state reaction	300 W Xe ($\lambda > 300$ nm)	Pure water	0.24 wt% NiO/ 20.7[f]	0.24 wt% NiO/ 9.5[f]	–	[48] (2002)
$AgNbO_3$	Solid-state reaction	300 W Xe ($\lambda > 300$ nm)	Mixture of H_2O vapor (20 Torr) and CH_4 (70 Torr) with Ar carrier/0.05 M $AgNO_3$	0.1 wt% Pt/38[f]	—/240[f]	–	[48] (2002)
(Cr,Sb)-codoped $SrTiO_3$ (0.5)	Solid-state reaction	300 W Xe ($\lambda > 420$ nm)	8 vol % CH_3OH/0.05 M $AgNO_3$	0.3 wt% Pt/78[f]	—/0.9[f]	–	[49] (2002)
La-doped $NaTaO_3$[e]	Solid-state reaction	400 W Hg	1 mM NaOH	0.2 wt% NiO/ 19800	0.2 wt% NiO/ 9660	56 (270)	[50] (2003)
$LaInO_3$ (0.25)[e]	Solid-state reaction	200 W Hg–Xe	Pure water	1 wt% RuO_2/ ~1.25[f]	1 wt% RuO_2/ ~0.5[f]	–	[51] (2003)
$BaIn_{0.5}Nb_{0.5}O_3$ (0.5)[e]	Solid-state reaction	400 W Hg	Pure water	1 wt% NiO_x/27.0[f]	1 wt% NiO_x/12.3[f]	–	[52] (2003)
$SrIn_{0.5}Nb_{0.5}O_3$ (0.5)[e]	Solid-state reaction	400 W Hg	Pure water	1 wt% NiO_x/13.8[f]	–	–	[52] (2003)
$CaIn_{0.5}Nb_{0.5}O_3$ (0.5)[e]	Solid-state reaction	400 W Hg	Pure water	1 wt% NiO_x/14.8[f]	–	–	[52] (2003)
$CaCo_{1/3}Nb_{2/3}O_3$ (0.5)[e]	Solid-state reaction	300 W Xe ($\lambda > 420$ nm)	Pure water	1 wt% NiO_x/0.86[f]	–	–	[53] (2003)
$SrCo_{1/3}Nb_{2/3}O_3$ (0.5)[e]	Solid-state reaction	300 W Xe ($\lambda > 420$ nm)	Pure water	1 wt% NiO_x/0.86[f]	–	–	[53] (2003)
$BaCo_{1/3}Nb_{2/3}O_3$ (0.5)[e]	Solid-state reaction	300 W Xe ($\lambda > 420$ nm)	Pure water	1 wt% NiO_x/1.37[f]	–	–	[53] (2003)
$BaZn_{1/3}Nb_{2/3}O_3$ (0.5)	Solid-state reaction	400 W Hg	13.5 vol% CH_3OH	0.5 wt% Pt/708.21[f]	–	–	[54] (2004)
		400 W Hg	13.5 vol% CH_3OH	0.5 wt% Pt/194.84[f]	–	–	

Table 1 (*continued*)

Photocatalyst (mass)	Preparation strategy	Lamp (filter)[a]	Reactant solution[b]	Activity/ μmol h^{-1} g_{cat}^{-1}[c]		AQY/% (wavelength/nm)[d]	Reference (year)
				Cocatalyst/H_2	Cocatalyst/O_2		
$BaZn_{1/3}Ta_{2/3}O_3$ (0.5)	Solid-state reaction						[54] (2004)
Rh-doped $SrTiO_3$ (0.3)	Solid-state reaction	300 W Xe ($\lambda > 440$ nm)	10 vol% CH_3OH	0.1 wt% Pt/117[f]	–	5.2 (420)	[55] (2004)
(Cr,Ta)-codoped $SrTiO_3$ (1)	Solid-state reaction	300 W Xe ($\lambda > 440$ nm)	6.5 vol% CH_3OH				[56] (2004)
$BaNi_{1/3}Nb_{2/3}O_3$ (0.5)	Solid-state reaction	400 W Hg	13.5 vol% CH_3OH	0.5 wt% Pt/68.22[f]	–	–	[54] (2004)
$BaNi_{1/3}Ta_{2/3}O_3$ (0.5)	Solid-state reaction	400 W Hg	13.5 vol% CH_3OH	0.5 wt% Pt/42.16[f]	–	–	[54] (2004)
$BaZn_{1/3}Nb_{2/3}O_3$ (0.5)[e]	Solid-state reaction	400 W Hg	Pure water	1.0 wt% NiO_x/ 291.22[f]	1.0 wt% NiO_x/ 145.61[f]	–	[57] (2004)
(Ni,Ta)-codoped $SrTiO_3$ (0.3)	Solid-state reaction	300 W Xe ($\lambda > 420$ nm)	10 vol% CH_3OH/0.05 M $AgNO_3$	0.1 wt Pt/2.4[f]	0.1 wt% Pt/0.5[f]	–	[58] (2005)
Cyanocobalamin/ $K_{0.95}Ta_{0.92}Zr_{0.08}O_3$ (0.1)[e]	Solid-state reaction	500 W Xe	KOH (pH = = 10.5)	0.2 wt% Pt/575.0	0.2 wt% Pt/280.4	12.2 (300)	[59,60] (2006, 2009)
$Fe_2O_3/SrTiO_3$	Hydrothermal reaction	250 W Oriel Arc Lamp ($\lambda \geq 420$ nm)	8% CH_3OH	—/85	–	–	[61] (2006)
$BiFeO_3/SrTiO_3$	Hydrothermal reaction	250 W Oriel Arc Lamp ($\lambda \geq 420$ nm)	8% CH_3OH	—/129	–	–	[61] (2006)
$NaTaO_3$ (1)[e]	Sol–gel reaction	400 W Hg	Pure water	—/1940	Stoichiometric ratio	–	[30] (2006)
$BaCo_{1/3}Nb_{2/3}O_3$ (0.2)	Sol–gel reaction	300 W Xe ($\lambda > 420$ nm)	18.5 vol% CH_3OH	0.5 wt% Pt/18.1	–	–	[62] (2006)
$LiNbO_3$ (0.1)	Wet-chemical method	400 W Hg	12.5 vol% CH_3OH	0.5 wt% Pt/4910[f]	–	–	[63] (2006)
Cr-doped $SrTiO_3$ (0.25)	Solid-state reaction	300 W Hg ($\lambda \geq 420$ nm)	13.5 vol% CH_3OH	0.4 wt% Pt/21[f]	–	0.86 (420.4)	[39] (2006)
$SrSnO_3$ (0.2)	Hydrothermal reaction	400 W Hg	13.5 vol% CH_3OH /0.0135 M $AgNO_3$	0.5 wt% Pt/8.2	—/2.5	4.6 (300)[g]	[64] (2007)
$NaTaO_3$ (1)[e]	Sol–gel reaction	400 W Hg	Pure water	—/2050	Stoichiometric ratio	–	[65] (2007)
$NaNbO_3$ (0.1)	Hydrothermal synthesis	350 W Hg	5 vol% CH_3OH	—/950	–	–	[66] (2007)
$KNbO_3$ (0.1)	Hydrothermal synthesis	350 W Hg	5 vol% CH_3OH	—/100	–	–	[66] (2007)
$NaTaO_3$ (0.1)	Hydrothermal synthesis	350 W Hg	5 vol% CH_3OH	—/36750	–	–	[66] (2007)
$KTaO_3$ (0.1)	Hydrothermal synthesis	350 W Hg	5 vol% CH_3OH	—/1040	–	–	[66] (2007)
Sr-doped $BaSnO_3$ (0.2)	Polymerized complex method	400 W Hg	Pure water	1.0 wt % RuO_2/44[f]	–	–	[67] (2007)

$NaTaO_3$–$LaCoO_3$ (0.5)	Solid-state reaction	300 W Xe ($\lambda > 420$ nm)	18.5 vol% CH_3OH	0.2 wt% Pt/~4.34[f]	–	–	[34] (2007)
$KNbO_3$/CdS (0.2)	Solid-state reaction	500 W Hg–Xe lamp ($\lambda > 400$ nm)	30 vol% isopropanol	0.1 wt% (Ni/NiO)/150	–	4.4 ($\lambda > 400$)	[68] (2008)
$BiFeO_3$ (0.1)	Microwave hydrothermal reaction	500 W Hg ($\lambda \geq 420$ nm)	4 mM $FeCl_3$	–	—/~0.75[f]	–	[69] (2008)
$BaZrO_3$ (0.2)[e]	Sol–gel reaction	400 W Hg	Pure water	—/104.5[f]	—/26.2[f]	3.7 (200)	[70] (2008)
TiO_2/$SrTiO_3$ (0.2)	Solid-state reaction	150 W Hg	4 M HCOOH	—/43.78[f]	–	–	[71] (2008)
TiO_2/$CaTiO_3$ (0.2)	Solid-state reaction	150 W Hg	3 M isopropanol	—/13.02[f]	–	–	[71] (2008)
TiO_2/$BaTiO_3$ (0.2)	Solid-state reaction	150 W Hg	3 M isopropanol	—/5.87[f]	–	–	[71] (2008)
$SrTiO_3$ (0.06)	Sol–gel reaction	500 W Hg	41.7 vol% CH_3OH	0.32 wt% Pt/3200	–	–	[72] (2008)
$SrTi_xM_{1-x}O_3$ (M = Ru, Rh, ir, Pt, Pd) (0.2)	Hydrothermal reaction	450 W Hg ($\lambda > 420$ nm)	10 vol% CH_3OH	1 wt% Pt/15.6[f]	–	–	[73] (2008)
$FeGaO_3$ (0.5)	Solid-state reaction	450 W Xe ($\lambda > 420$ nm)	0.5 M KOH with 2.5 mL min^{-1} H_2S flow	1 wt% NiO_x/2495[f]	–	9.3 (550)	[74] (2008)
$KNbO_3$ (0.2)	Hydrothermal reaction	400 W Hg	11.9 vol% CH_3OH	0.5 wt% Pt/5170	–	–	[75] (2008)
$SrTiO_3$–$LaTiO_2N$ (0.15)	NH_3 nitridation	300 W Xe ($\lambda > 420$ nm)	18.5 vol% CH_3OH solution/0.01 M $AgNO_3$	3 wt% Pt/10[f]	3 wt% Pt/8[f]	–	[76] (2008)
$AgSbO_3$ (0.5)	Solid-state reaction	300 W Xe ($\lambda > 400$ nm)	0.0185 M $AgNO_3$	–	—/74[f]	–	[77] (2008)
Sr-doped $NaTaO_3$ (0.5)[e]	Solid-state reaction	400 W Hg	Pure water	0.1 wt% NiO/13600[f]	0.1 wt% NiO/6690[f]	–	[78] (2009)
Ba-doped $NaTaO_3$ (0.5)[e]	Solid-state reaction	400 W Hg	Pure water	0.2 wt% NiO/9780[f]	0.2 wt% NiO/4780[f]	–	[78] (2009)
Ca-doped $NaTaO_3$ (0.5)[e]	Solid-state reaction	400 W Hg	Pure water	0.2 wt% NiO/4930[f]	0.2 wt% NiO/2600[f]	–	[78] (2009)
$NaTaO_3$ (1)[e]	Sol–gel reaction	400 W Hg	Pure water	—/~2600	—/~1300	–	[79] (2009)
Cu-doped $AgNbO_3$ (0.1)	Liquid–solid method	300 W Xe ($\lambda > 420$ nm)	0.005 M $AgNO_3$	–	—/9.9[f]	–	[80] (2009)
$AgNbO_3$–$SrTiO_3$ (0.5)	Solid-state reaction	300 W Xe ($\lambda \geq 410$ nm)	0.0185 M $AgNO_3$	–	—/162[f]	16.4 (420.4)	[35,36] (2008, 2009)
Na-doped $SrTiO_3$ (0.3)[e]	Solid-state reaction	450 W Hg	Pure water	0.5 wt% Rh_2O_3+0.5 wt% Cr_2O_3/~6.6[f]	0.5 wt% Rh_2O_3+0.5 wt% Cr_2O_3/~3.3[f]	–	[81] (2009)
Sr-doped $NaTaO_3$ (0.5)	Solid-state reaction	400 W Hg	Pure water	—/1090[f]	–	–	[82] (2009)
$YInO_3$ (0.35)	Parallel solution combustion synthesis	300 W Xe	0.25 M Na_2S+0.25 M Na_2SO_3	0.5 wt% Pt/18.88	–	0.65 (420)	[37] (2009)

Table 1 (*continued*)

Photocatalyst (mass)	Preparation strategy	Lamp (filter)[a]	Reactant solution[b]	Activity/ $\mu mol\ h^{-1}\ g_{cat}^{-1}$[c]		AQY/% (wavelength/nm)[d]	Reference (year)
				Cocatalyst/H_2	Cocatalyst/O_2		
$Na(Bi_xTa_{1-x})O_3$ (0.1)	Hydrothermal reaction	350 W Hg ($\lambda > 400$ nm)	5 vol% CH_3OH	0.1 wt% NiO/ 59.48	–	–	[83] (2009)
$NaTaO_3$–$LaCrO_3$ (0.5)	Solid-state reaction	300 W Xe ($\lambda > 420$ nm)	18.5 vol% CH_3OH	0.2 wt% Pt/4.5[f]	–	0.5 (420)	[38] (2009)
$NaNbO_3$ (0.3)[e]	Complex-based synthesis	400 W Hg	Pure water	0.5% RuO_2/~21[f]	0.5% RuO_2/~10[f]	~6.6 (340)	[84] (2010)
$BaZr_{1-x}Sn_xO_3$ (0.2)[e]	Polymerized complex method	400 W Hg	Pure water	—/138[f]	—/37[f]	–	[85] (2010)
$CaTiO_3$ (2.5)	Solid-state reaction	300 Xe	Mixture of H_2O vapor (1.5%) and CH_4 (50%) with Ar carrier	0.04 wt%/ 0.48 $\mu mol\ min^{-1}$			[86] (2010)
TiO_2/$SrTiO_3$	Hydrothermal reaction	Low-pressure UVP Pen-Ray Hg	11.1 vol% CH_3OH	—/386.6[f]	–	0.854 (254)	[87] (2010)
$NaTaO_3$ (1)[e]	Sol–gel reaction	400 W Hg	Pure water	3 wt% NiO/9000	3 wt% NiO/4500	6.4 (310)	[88] (2010)
Sr_2AlNbO_6 (0.5)	Solid-state reaction	100 W Hg	10 vol% CH_3OH/0.01 M AgF	1 wt% RuO_2/26.7[f]	1 wt % RuO_2// 21.6[f]	–	[89] (2010)
$CaTi_{1-x}Cu_xO_3$ (0.1)	Sol–gel reaction	350 W Xe ($\lambda > 400$ nm)	5 vol% CH_3OH	—/22.7	–	–	[90] (2010)
$LaNi_{0.7}Cu_{0.3}O_3$ (0.1)	Sol–gel reaction	125 W Xe ($\lambda > 400$ nm)	12.5 vol% HCHO	—/583	–	2.98	[91] (2010)
Eosin Y/$SrTiO_3$ (0.2)	Sol–gel reaction	300 W Xe ($\lambda > 400$ nm)	15 vol% DEA+0.5 mM E.Y.	0.5 wt% Pt/60.3[f]	–	–	[92] (2010)
$SrTiO_3$ (0.2)	Sol–gel reaction	300 W Xe ($\lambda > 400$ nm)	50 vol% CH_3OH	1 wt% Au/200[f]	–	–	[93] (2010)
$LaNi_{1-x}Cu_xO_3$ (0.1)	Polymerized complex method	125 W Xe ($\lambda > 400$ nm)	12.5 vol% CH_3OH	—/1180	–	–	[94] (2010)
La-doped $NaTaO_3$ (1)	Solid-state reaction	300 W Xe	Mixture of H_2O vapor (1.5%) and CH_4 (50%) with Ar carrier	0.03 wt% Pt/ 4.5 $\mu mol\ min^{-1}$	–	30 (240–270)	[95] (2010)
In_2O_3/$NaNbO_3$ (0.3)	Coprecipitation method	400 W Hg	18.5 vol% CH_3OH	0.8 wt% Pt/~42.9	–	1.45 (420)	[96] (2010)
$ZnFe_2O_4$/$SrTiO_3$ (0.25)	Solid-state reaction	200 W tungsten	0.025 M $Na_2S_2O_3$	9.2 $cm^3\ h^{-1}\ mg_{cat}^{-1}$[c]	–	–	[97] (2010)
$LaFeO_3$ (0.05)	Sol–gel reaction	125 W Hg ($\lambda > 420$ nm)	10 vol% CH_3OH/0.05 M $AgNO_3$	—/430[f]	—/213[f]	8.07 (visible light)	[98] (2010)
$BaZrO_3$–$BaTaO_2N$ (0.5)	Polymerized complex method	300 W Xe ($420 < \lambda < 800$ nm)	4 mM NaI	0.3 wt% Pt/~0.9[f]	–	–	[99] (2011)
(Na,K)TaO_3 (0.1)[e]	Molten-salt method	350 W Hg	Pure water	—/2510[f]	—/340[f]	–	[100] (2011)
Hf-doped (Na,K)TaO_3 (0.1)[e]	Molten-salt method	350 W Hg	Pure water	—/4960[f]	—/2460[f]	–	[100] (2011)
	Sol–gel reaction	400 W Hg	Pure water	—/1057[f]	—/530[f]	2.8 (310)	

$Na_{1-x}K_xTaO_3$ (0.1)[e]							[31] (2011)
$Na_{0.5}La_{0.5}TiO_3$–$LaCrO_3$ (0.3)	Hydrothermal method	300 W Xe ($\lambda > 420$ nm)	18.5 vol% CH_3OH	1 wt% Pt/8.2	–	–	[101] (2011)
Cr-doped $SrTiO_3$ (0.25)	Sol–gel hydrothermal synthesis	300 W Xe ($\lambda > 420$ nm)	18.5 vol% CH_3OH	0.6 wt% Pt/82.6[f]	–	2.95 (410)	[102] (2011)
$Na_{1-x}La_xTaO_3$ (0.5)[e]	Sol–gel reaction	400 W Hg ($\lambda \geq 250$ nm)	Pure water	0.3 wt% (Ni/NiO)/3450	Stoichiometric ratio	–	[103] (2011)
$NaTaO_3$ (0.3)[e]	Confined space synthesis	450 W Hg	Pure water	1 wt% NiO/2000[f]	1 wt% NiO/1000[f]	–	[104] (2011)
$LiNbO_3$ (0.3)[e]	Complex-based synthesis	400 W Hg	Pure water	0.5 wt% RuO_2/31[f]	0.5 wt% RuO_2/17[f]	0.7 (254)	[105] (2011)
$AgNbO_3$–$NaNbO_3$ (0.1)[e]	Molten salt treatment	300 W Xe ($\lambda > 400$ nm)	10 vol% CH_3OH/0.02 M $AgNO_3$	0.3 wt% Pt/~0.2[f]	—/~4.6[f]	–	[106] (2011)
La-doped $NaTaO_3$ (0.5)	Sol–gel reaction	400 W Hg ($\lambda > 250$ nm)	10 vol% CH_3OH	—/1430[e]	–	–	[107] (2011)
C_3N_4/$SrTiO_3$ (0.2)	Coprecipitation method	250 W iron-doped metal halide ($\lambda > 420$ nm)	0.025 M oxalic acid	1 wt% Pt/440	–	–	[108] (2011)
(Cr,Ta)-codoped $SrTiO_3$	Spray pyrolysis	300 W Xe ($\lambda > 415$ nm)	20 vol% CH_3OH	1 wt% Pt/423.6[f]	–	–	[109] (2011)
Ag-doped $SrTiO_3$	Hydrothermal method	350 W Hg	10 vol% CH_3OH	6.61 mmol m^{-2} h^{-1}	–	–	[110] (2011)
$GaFeO_3$ (0.05)	Sol–gel reaction	300 W Xe ($\lambda > 395$ nm)	Pure water	—/36.1[f]	–	~0.13 (450)	[111] (2012)
Sr_xNbO_3	Solid-state method	250 W iron-doped metal halide ($\lambda \geq 420$ nm)	0.02 M oxalic acid/0.005 M $AgNO_3$	1 wt%/44.8	—/~2.5[f]	–	[13] (2012)
$AgSbO_3$ (0.3)	Hydrothermal reaction	300 W Xe ($\lambda > 420$ nm)	0.0185 M $AgNO_3$	–	—/138	–	[112] (2012)
(La,Cr)-codoped $SrTiO_3$ (0.3)	Sol–gel hydrothermal reaction	300 W Xe ($\lambda > 400$ nm)	18.5 vol% CH_3OH+5 M NaOH	—/326.8[f]	–	25.6 (425)	[113] (2012)
(Cr,Ta)-codoped $SrTiO_3$ (0.3)	Hydrothermal reaction	300 W Xe ($\lambda > 420$ nm)	18.5 vol% CH_3OH	0.5 wt% Pt/~2[f]	–	–	[114] (2012)
$LaCoO_3$ (0.25 g L^{-1})	Sol–gel reaction	Xe ($\lambda > 420$ nm)	5.0 mM $Na_2S_2O_8$+0.25 mM $[Ru(bpy)_3](ClO_4)$+50 mM phosphate buffer solution (pH = = 7.0)	–	11 μmol s^{-1} g^{-1}	0.16 (450)	[40] (2012)
Er-doped $SrTiO_3$ (0.3)	Polymerized complex method	300 W Xe ($\lambda > 420$ nm)	0.35 M Na_2S+0.25 M Na_2SO_3/0.0185 M $AgNO_3$	1 wt% Pt/46.23	—/44.23	0.03/0.04 (>420) for H_2/O_2 evolution, respectively	[115] (2012)
$CaTaO_2N$–$CaZrO_3$ (0.1)	Polymerized complex method	300 W Xe ($\lambda > 420$ nm)	11.1 vol% HCOOH	1 wt% Pt/5.24[f]	–	–	[116] (2012)
(Ni,Ta)-codoped $SrTiO_3$ (0.1)	Spray pyrolysis process	300 W Xe ($\lambda > 415$ nm)	20 vol% CH_3OH	1 wt% Pt/561.2	–	–	[117] (2012)
$NaBi_xTa_{1-x}O_3$ (0.1)	Spray pyrolysis process	300 W Xe ($\lambda > 415$ nm)	20 vol% CH_3OH	0.2 wt% NiO/1355	–	–	[118] (2012)
		500 W Xe	20 vol% CH_3OH	3 wt% Pt/369.8	–	1.45 (346)	

Table 1 (*continued*)

Photocatalyst (mass)	Preparation strategy	Lamp (filter)[a]	Reactant solution[b]	Activity/ μmol h^{-1} g_{cat}^{-1}[c]		AQY/% (wavelength/nm)[d]	Reference (year)
				Cocatalyst/H_2	Cocatalyst/O_2		
$Na_{0.5}Bi_{0.5}TiO_3$ (0.15)	Hydrothermal reaction						[119] (2012)
Bi-doped $NaTaO_3$ (0.05)	Solid-state reaction	800 W Xe ($\lambda > 390$ nm)	20 vol% CH_3OH	0.06 wt% Pt/0.86	–	–	[120] (2012)
$NaNbO_3$ (0.3)	Polymerized complex method	300 W Xe ($\lambda > 300$ nm)	18.5 vol% CH_3OH	0.5 wt% Pt/156.1[f]	–	–	[32] (2012)
TiO_2/$SrTiO_3$ (0.5 Mg ML^{-1})	Hydrothermal reaction	400 W Hg	CH_3OH	—/~550[f]	–	–	[121] (2012)

[a] The lamp (with filter if necessary) was used as light source.
[b] Aqueous solution unless otherwise specified.
[c] g_{cat}^{-1} represented "per gram photocatalyst", and mg_{cat}^{-1} represented "per milligram photocatalyst".
[d] AQY represented "apparent quantum yield".
[e] The photocatalyst was used for overall water splitting.
[f] The rate unit of gas evolution was μmol h^{-1}.
[g] 200 W Hg–Xe lamp was used.

The band gaps of $AgTaO_3$ and $AgNbO_3$ were 3.4 and 2.8 eV, respectively, being 0.6 eV smaller than the band gaps of $NaTaO_3$ and $NaNbO_3$, both of which only had UV-light response. It was found that a hybrid orbital of Ag 4d and O 2p formed a valence band at a more negative level than O 2p orbitals. $AgNbO_3$ has arisen as a new visible-light-driven photocatalyst possessing the ability to evolve H_2 or O_2 from water in the presence of sacrificial reagents [48].

Sato et al. reported the ability of $NaSbO_3$ photocatalyst for overall water splitting. However, this material was only active under UV-light irradiation due to the wide bandgaps (about 4.4 eV) [44,45]. Based on the electronic configuration of Ag^+, Kako et al. prepared $AgSbO_3$ photocatalyst with an absorption edge up to about 480 nm and successfully applied for visible-light-driven O_2 evolution from an aqueous silver nitrate solution [77]. Band-structure calculation revealed that the conduction-band minimum (CBM) and valence-band maximum (VBM) of $NaSbO_3$ were composed of Sb 5s and O 2p orbitals, respectively [44,129], whereas for $AgSbO_3$, the CBM consisted of the hybridized Ag 4d and O 2p orbitals, and VBM mainly consisted of the Ag 5s and the Sb 5s orbitals. Consequently, The Ag^+ largely contributed to the bandgap narrowing by lifting up the valance band.

Ion replacement was proved as an effective method to construct new energy bands in ABO_3 photocatalysts and thus to extend the light response range.

4.1.3. Multi-component solid solution

Designing solid solutions between end-member materials with analogous crystal structures but different electronic band structures has greatly promoted the development of photocatalysts in recent years [4,41]. On account of the highly susceptible substitution of different cations at both A and B sites of ABO_3-type perovskite oxides [39,130], the derived solid solutions with versatile properties are noteworthy [34–36,38,83,106].

Due to the excellent photocatalytic performance of $SrTiO_3$ and $NaTaO_3$ for overall water splitting under UV irradiation [50,123] and the inability of the two materials for harnessing visible light, a series of $SrTiO_3$- and $NaTaO_3$-based solid-solution photocatalysts, such as $SrTiO_3$–$AgNbO_3$ [35,36], $NaTaO_3$–$LaCoO_3$ [34], $NaTaO_3$–$LaCrO_3$ [38], and $NaTaO_3$–$NaBiO_3$ [83], were developed and successfully applied to photocatalytic H_2 or O_2 evolution under visible-light irradiation. A novel series of solid-solution semiconductors $SrTiO_3$–$AgNbO_3$ have been developed by Wang et al. as highly visible-light-active photocatalysts for efficient O_2 evolution. The mixed valent perovskites $(AgNbO_3)_{1-x}(SrTiO_3)_x$ possess a modulated energy band structure. The conduction band is composed of the hybrid (Ti 3d+Nb 4d) orbitals and the valence band is constructed by the hybrid (O 2p+Ag 4d) orbitals. The modulation of band structure (band gap energy, band edge positions, etc.) depends on the extent of orbital hybridization. As a result of competition between the absorption ability to visible-light and the reductive/oxidative abilities, the highest visible-light activities for O_2 evolution are realized over $(AgNbO_3)_{0.75}(SrTiO_3)_{0.25}$. It was proved that making solid-solution oxide semiconductors with tunable electronic structures is a feasible band engineering approach for the development of highly visible-light-active photocatalysts.

Cubic perovskite $Na_{0.5}La_{0.5}TiO_3$ has too wide a bandgap to utilize visible light [131]. The analogous perovskite $LaCrO_3$ has a bandgap narrow enough to absorb visible light [132,133] but was reported to show trace amounts of H_2 evolved by visible-light-driven photocatalysis [38] since the conduction band level is relatively low and thus the driving force for reducing H_2O to H_2 is weakened. In our recent work, novel cubic perovskite structure photocatalyst of $Na_{0.5}La_{0.5}TiO_3$–$LaCrO_3$ solid-solution single-crystal nanocubes were prepared by means of facile, surfactant-free hydrothermal reactions at 180 °C for 48 h for the first time, and successfully applied to visible-light-driven photocatalytic H_2 evolution. The introduction of $LaCrO_3$ component into $Na_{0.5}La_{0.5}TiO_3$ rendered the further distortion of BO_6 octahedra in ABO_3, thus beneficial for the excitation, separation and migration of photogenerated charge carriers. The bandgap was dramatically narrowed by Cr^{3+} from 3.19 ($Na_{0.5}La_{0.5}TiO_3$, i.e., NaLaTi) to 2.25 eV ($(Na_{0.5}La_{0.5}TiO_3)_{1.00}(LaCrO_3)_{0.08}$, i.e., NaLaTi–0.08Cr), thereby enabling the utilization of visible light (< 550 nm). The narrowing of the bandgap was reasonably explained by the band-structure calculations (see Fig. 2). The new CBM was composed of Cr 3d eg orbitals and Ti 3d orbitals, and the new VBM was formed by Cr 3d t2g orbitals rather than O 2p orbitals (see Fig. 3). The solid-solution configuration maintained the charge balance to preserve the valence of Cr^{3+} rather than Cr^{6+}, and accommodated Cr^{3+} with high content to form new energy bands instead of localized impurity levels. The hydrothermal preparation strategy ensured the formation of single crystals with high purity, few defects, and regulated morphology; it also guaranteed the valences of Ti^{4+} and Cr^{3+} in the solid solution. Consequently, owing to the solid-solution configuration and hydrothermal preparation strategy, the recombination of photogenerated carriers could be effectively suppressed to benefit photocatalytic H_2 evolution. $(Na_{0.5}La_{0.5}TiO_3)_{1.00}(LaCrO_3)_{0.08}$ solid-solution single-crystal nanocubes showed stable visible-light-driven photocatalytic activity for H_2 evolution (rate, 8.2 μmol h^{-1} g_{cat}^{-1}) in methanol aqueous solution (see Fig. 4) [101].

In addition to solid solutions between two ABO_3 end-member materials, solid solutions between end-member materials of one ABO_3 and one ABX_3 perovskite oxynitride, such as $SrTiO_3$–$LaTiO_2N$ [76], $BaZrO_3$–$BaTaO_2N$ [99], and $CaZrO_3$–$CaTaO_2N$ [116], were also designed by different research groups, aiming to lift up valence band and thus to narrow the bandgaps of ABO_3 materials by incorporating N to take part in the formation of valence band. $SrTiO_3$–$LaTiO_2N$ showed photocatalytic activities for H_2 and O_2 evolution in corresponding sacrificial reagents under visible light irradiation. The band gaps of $(SrTiO_3)_{1-x}(LaTiO_2N)_x$ reduced from 3.18 to 2.04 eV with increasing x from 0 to 0.30. Moreover, the calculated results suggested that the band gap narrowing came from the hybridization of N 2p and O 2p orbital. Matoba et al. reported a solid solution between $BaTaO_2N$ and $BaZrO_3$. Compared with that of $BaTaO_2N$, the photocatalytic activity of $BaZrO_3$–$BaTaO_2N$ was

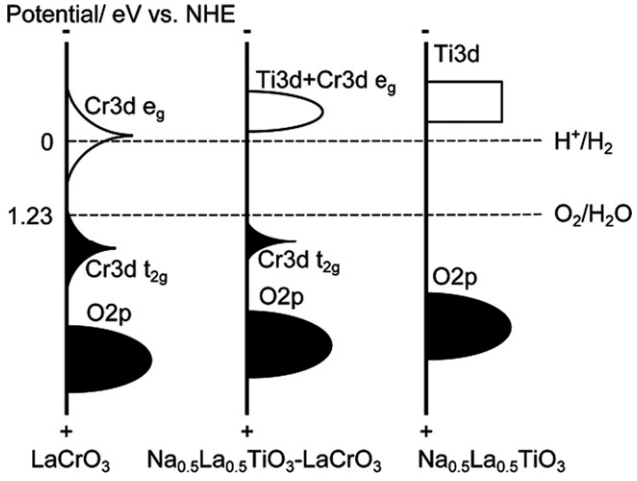

Fig. 3 Schematic band structures of $LaCrO_3$, $Na_{0.5}La_{0.5}TiO_3$–$LaCrO_3$ solid solution, and $Na_{0.5}La_{0.5}TiO_3$. Reprinted with permission from Ref. [101].

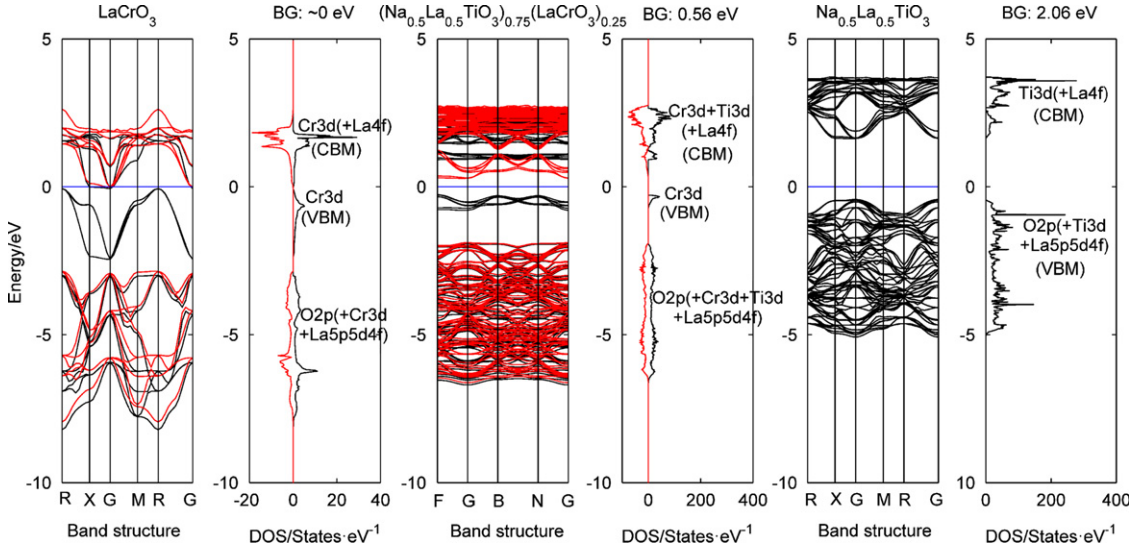

Fig. 2 Electronic band structures and total density of states (TDOS) near the Fermi levels for $LaCrO_3$, $Na_{0.5}La_{0.5}TiO_3$–$LaCrO_3$ solid solution, and $Na_{0.5}La_{0.5}TiO_3$ calculated by density functional theory (dark and red lines: results from two different spin polarization direction; blue lines: Fermi levels). Reprinted with permission from Ref. [101].

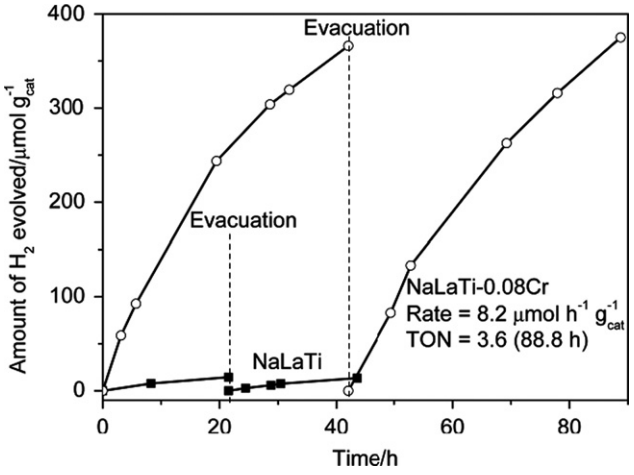

Fig. 4 Time courses of visible-light-driven H_2 evolution on photocatalysts of as-prepared NaLaTi (solid squares) and NaLaTi–0.08Cr (open circles). Reprinted with permission from Ref. [101].

improved six- to nine-fold for H_2 evolution in aqueous NaI solution under visible-light irradiation due to an increased driving force for surface redox reactions and fewer defects [99]. The analogous solid solution of $CaZrO_3$–$CaTaO_2N$ was prepared almost at the same time, and exhibit photocatalytic activity for H_2 evolution from formic acid aqueous solution under visible-light irradiation. The narrow band gap, sufficient crystallization, enough pore volume and large specific surface area resulted in the best photocatalytic activity of $(CaZrO_3)_{0.2}(CaTaO_2N)_{0.8}$ [116].

Consequently, the solid-solution construction was demonstrated to be a powerful strategy to design ABO_3-based photocatalysts, and exhibited the following merits. The band structures of photocatalysts could be optimized to mediate the competition between the absorption ability to visible-light and the reductive/oxidative abilities. The unfavorable valence states of multivalent metal cations and the lattice defects could be depressed to reduce the recombination of photogenerated charge carriers.

4.1.4. *Multi-component composites*

Synergistic effect on photocatalytic performance could be achieved when different materials were combined to form multi-component composites [19,25,134,135]. The ABO_3-based multi-component composites mainly include metal–ABO_3 composites [103,110,136], semiconductor–ABO_3 composites [61,87,96,97,108,121] and dye–ABO_3 composites [59,60,92]. The other components couple with ABO_3 generally functioned as cocatalysts or photosensitizers.

Domen et al. designed $SrTiO_3$ photocatalyst loaded with the classical NiO/Ni double-layer cocatalyst by reduction/oxidation pretreatment for overall water splitting. H_2 evolution occurs over NiO while O_2 evolution takes place over $SrTiO_3$, thus announced the separation of reactive sites for H_2 and O_2 evolution, respectively. Furthermore, the existence of metallic Ni between the interface of NiO and $SrTiO_3$ facilitated the transfer of electrons between both materials, and therefore enhanced the photocatalytic activity [136]. Moreover, Hu and Teng investigated the interaction between NiO cocatalyst with $NaTaO_3$ photocatalyst for overall water splitting under UV illumination. Activity increased significantly with NiO loading and reached a maximum at first, and then decreased with further loading. It was found that the interdiffusion of Na^+ and Ni^{2+} cations created a solid-solution transition zone ($Na_xNi^{2+}_{1-2x}Ni^{3+}_xO$ and $Ni_xNa_{1-x}TaO_3$) on the outer sphere of $NaTaO_3$ (see Fig. 5). For less NiO contents, no NiO clusters appeared on the $NaTaO_3$ surface, and the reduction/oxidation pretreatment did not enhance photocatalytic activity. The high activity resulting from a low NiO loading suggests that the interdiffusion of cations heavily doped the p-type NiO and n-type $NaTaO_3$, reducing the depletion widths and facilitating charge transfers through the interface barrier [88]. By comparing the above results, It could be found that NiO was an excellent cocatalyst loaded on ABO_3 photocatalysts for overall water splitting, but the mechanisms for activity enhancement were different due to the different structural features, which were considerably affected by the interaction between cocatalyst and photocatalyst host. Further research on Ni/NiO cocatalyst loaded on ABO_3 photocatalysts (such as Ni/NiO/$Na_{1-x}La_xTaO_3$ [103] and Ni/NiO/$KNbO_3$/CdS [68]) for H_2 evolution was also performed in other groups. In addition to NiO, other cocatalysts, such as metallic Ag [110], Au, Pt, Ag, Ni, Ce, and Fe [93] were also employed to collect photogenerated electrons and thus to promote photocatalytic H_2 evolution.

Heterojunctions could be formed by coupling other band structure-matched semiconductors with ABO_3 photocatalysts to accelerate the separation of photogenerated charge carriers.

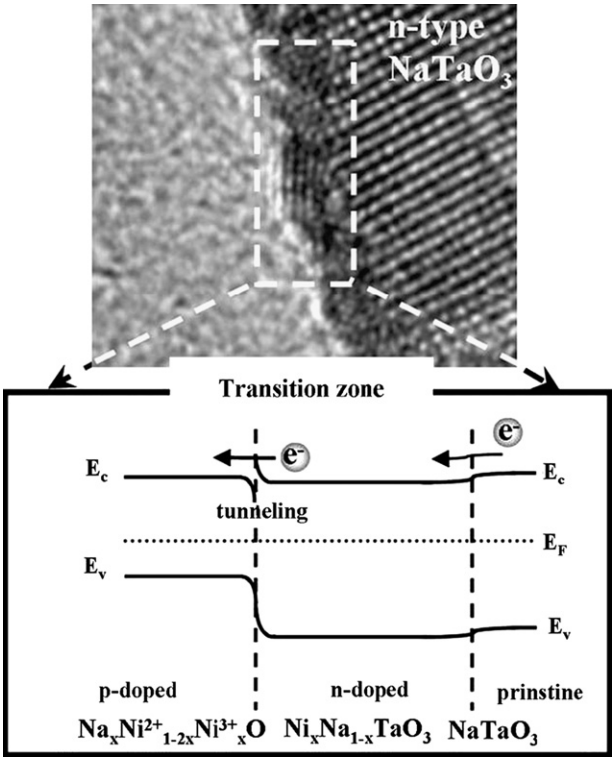

Fig. 5 Schematic energy-level diagrams of the NiO and $NaTaO_3$ contact with interdiffusion of Ni^{2+} and Na^+ to form p-doped NiO (i.e., $Na_xNi^{2+}_{1-2x}Ni^{3+}_xO$) and n-doped $NaTaO_3$ (i.e., $Ni_xNa_{1-x}TaO_3$) at the interface. Steeper band bending and reduced depletion widths appeared at the heterojunction interface. E_c, E_v, and E_F represent the energy positions of the conduction band edge, valence band edge, and Fermi level, respectively. Reprinted with permission from Ref. [88].

$TiO_2/SrTiO_3$ heterostructures were prepared by different groups [87,121]. Ng et al. reported that in comparison to the respective pristine semiconductor photocatalysts, the heterostructured $TiO_2/SrTiO_3$ film showed the highest efficiency in photocatalytic splitting of water to produce H_2, 4.9 times that of TiO_2 and 2.1 times that of $SrTiO_3$. The enhanced photocatalytic efficiency is largely attributed to the efficient separation of photogenerated charges at heterojunctions of the two dissimilar semiconductors, as well as a negative redox potential shift in the Fermi level. Furthermore, the coupled semiconductors with ABO_3 photocatalysts could act as photosensitizers to harness low-energy photons that could not be utilized by the ABO_3 host due to the wide bandgaps [61,96,97,108]. A series of $SrTiO_3$-based heterostructural photocatalysts (such as $SrTiO_3/Fe_2O_3$ $SrTiO_3/BiFeO_3$ [61], $ZnFe_2O_4/SrTiO_3$ [97], and $C_3N_4/SrTiO_3$ [108]) were developed and successfully applied to visible-light-driven H_2 evolution. Luo and Maggard reported that both $SrTiO_3/Fe_2O_3$ and $SrTiO_3/BiFeO_3$ systems exhibited visible-light photocatalytic activity, while pure $SrTiO_3$, Fe_2O_3, and $BiFeO_3$materials exhibit little visible-light activity. These results demonstrate that composite systems offer a unique and competitive approach to the visible-light activation of $SrTiO_3$ [61]. In addition to semiconductors, dyes (such as Eosin Y [92] and porphyrinoids [59,60]) were also employed as sensitizers to enhance the light response [92] and the separation of photogenerated charge carriers [59,60] on ABO_3 photocatalysts.

The above results demonstrated that constructing of ABO_3-based composites could not only accelerate the separation of photogenerated charge carriers by matching band structures in heterostructures, but also improve the utilization of incident light by photosensitization.

4.2. *Micro-/nano-structure adjustment*

Micro-/nano-structure adjustment of materials are generally achieved by employing appropriate preparation strategies [16,27,28,137–139]. As far as ABO_3-based photocatalysts are concerned, various preparation strategies were developed to adjust their micro-/nano-structures, aiming to optimize the photocatalytic process.

4.2.1. *Solid-state reaction*

Solid-state reaction is the most frequently used method to prepare ABO_3-based materials, but the high-temperature process generally resulted in as-prepared materials with defects and large particle sizes, which prompted the recombination of photogenerated carriers and thus led to low activity [64]. However, researchers from Kudo' group successfully prepared $NaTaO_3$-based photocatalysts with nanostep structure by solid-state reaction [43,50,78,82]. Doping of metal cations (including lanthanides [43,50] and alkaline earth metal ions [78,82]) played the key role in constructing such a unique micro-/nano-structure. Among La, Pr, Nd, Sm, Gd, Tb and Dy, La was the most active dopant to improve the photocatalytic activity for overall water splitting under UV irradiation [43,82]. NiO/La-doped $NaTaO_3$ (i.e., $NiO/NaTaO_3$:La) showed photocatalytic activity 9 times higher than nondoped $NiO/NaTaO_3$. The maximum AQY was 56% at 270 nm, thus setting the highest record for overall water splitting under UV irradiation. It was found that the particle sizes of La-doped $NaTaO_3$ crystals were smaller than that of the nondoped $NaTaO_3$ crystal and that the ordered surface nanostructure with characteristic steps was created by the lanthanum doping. The small particle size with a high crystallinity promoted the reaction of photogenerated electrons and holes with water molecules. NiO cocatalysts were loaded on the edge of the nanostep structure of La-doped $NaTaO_3$ photocatalysts as ultrafine particles. The H_2 evolution proceeded on the ultrafine NiO particles loaded on the edge while the O_2 evolution occurred at the groove of the nanostep structure. Consequently, the reaction sites for H_2 evolution were separated from those of O_2 evolution over the ordered nanostep structure. Both the small particle size and the ordered surface nanostep structure of the NiO/La-doped $NaTaO_3$ photocatalyst contributed to the highly efficient overall water splitting (see Fig. 6) [43].

4.2.2. *Hydrothermal/solvothermal reaction*

Hydrothermal/solvothermal synthesis was widely acknowledged as a powerful tool to generate products with high crystallinity and purity, few defects, and novel morphologies. The technological efficiency in developing bigger, purer, and dislocation-free single crystals is of much importance [140].

Chen and Ye successfully prepared dumbbell-like and rod-like $SrSnO_3$ nanostructures by a facile hydrothermal process and subsequent heat-treatment process. Compared with the sample from solid-state reaction, the as-prepared $SrSnO_3$ nanostructures showed higher activity for H_2 and O_2 evolution in corresponding sacrificial reagents under UV light irradiation due to the higher surface area and fewer defects [64]. Ding et al. synthesized $KNbO_3$ single-crystal nanowires by a hydrothermal method. The prepared nanowires achieved the highest photocatalytic activity in all reported $KNbO_3$

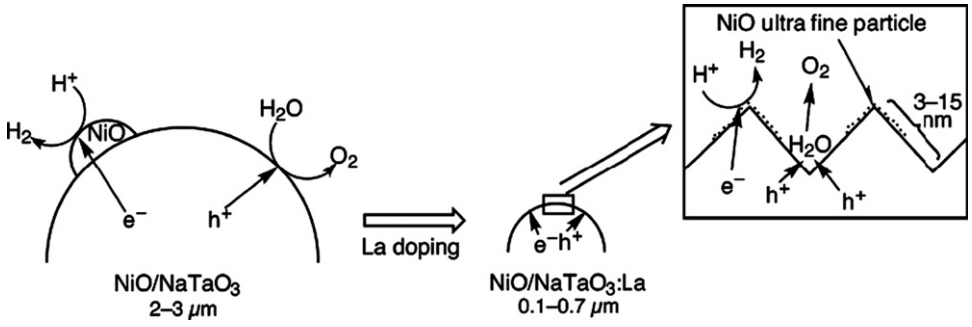

Fig. 6 Mechanism of highly efficient photocatalytic water splitting over $NiO/NaTaO_3$:La photocatalysts. Reprinted with permission from Ref. [50].

materials for H_2 evolution from aqueous CH_3OH solutions because of the high surface area and high crystallinity [75]. Yu et al. from the same group synthesized Cr-doped $SrTiO_3$ with high specific surface areas (19.3–65.4 $m^2 g^{-1}$), and good crystallinity, and small crystalline size (20–30 nm) by using a sol–gel hydrothermal method. The as-prepared Pt/Cr-doped $SrTiO_3$ photocatalyst exhibited H_2 evolution rate 3 times higher than that of the sample from solid-state reaction in methanol solution under visible light irradiation due to the high specific surface area and good crystallinity [102]. Joshi et al. synthesized $BiFeO_3$ single-crystal nanocubes via simple microwave-hydrothermal procedure in sizes of 50–200 nm and successfully applied to photocatalytic O_2 evolution in $FeCl_2$ solution. The microwave condition largely shortened the reaction time (only 30 min) [69]. The hydrothermal conditions have important effects on the physicochemical properties and photocatalytic performance of ABO_3 materials. Quaternary perovskite oxide $Na_{0.5}Bi_{0.5}TiO_3$ hierarchical microspheres was synthesized by Wang and Wang via a low-temperature hydrothermal route. The alkaline concentration played crucial roles in the physicochemical properties and the photocatalytic activities. $Na_{0.5}Bi_{0.5}TiO_3$ microspheres prepared with 9 M NaOH exhibited the highest rate of H_2 evolution under UV and visible light, because the highest conduction band edge and the smallest particle sizes led to the suppression of electron–hole recombination [119]. Using a three-dimensional mesoporous carbon as template to provide the confined space, Yokoi et al. prepared a colloidal array of $NaTaO_3$ nanoparticles in size of 20 nm and with a surface area of 34 $m^2 g^{-1}$ by a hydrothermal reaction. The colloidal array of $NiO/NaTaO_3$ nanoparticles showed photocatalytic activity for overall water splitting under UV irradiation more than three times as high as non-structured bulk $NaTaO_3$ particles [104].

The above results confirmed the advantages of hydrothermal/solvothermal reaction in preparing ABO_3-based photocatalysts with high crystallinity, few defects, small sizes, large surface areas, and special micro-/nano-structures.

4.2.3. *Spray pyrolysis process*

Spray pyrolysis process is an aerosol process to produce powders of highly uniform in morphology and composition because of short residence time and droplets of several micrometers in which precursors are distributed uniformly before evaporation and decomposition. Park et al. prepared a series of ABO_3-based photocatalysts (such as (Cr,Ta)-codoped $SrTiO_3$ [109], (Ni,M)-codoped $SrTiO_3$ (M = La or Ta) [117], and $NaBi_xTa_{1-x}O_3$ [118]) by this method. Compared with (Cr,Ta)-codoped $SrTiO_3$ photocatalyst prepared by solid-state reaction, the photocatalyst prepared by spray pyrolysis showed a higher (about 100 times) H_2 evolution rate and shorter (8 times) induction period in aqueous methanol solution under visible-light irradiation because of the increased surface roughness, compositional uniformity, and surface area, and the smaller amount of Cr^{6+} [109]. Another two photocatalysts, (Ni,La)-codoped $SrTiO_3$ and (Ni,Ta)-codoped $SrTiO_3$, were also prepared by continuous spray pyrolysis. Furthermore, solid-solution $NaBi_xTa_{1-x}O_3$ photocatalysts were prepared by spray pyrolysis process. Compared with that of photocatalyst prepared by the hydrothermal method, the H_2 evolution rate of $NaBi_xTa_{1-x}O_3$ photocatalysts from spray pyrolysis was enhanced almost 20 times in aqueous methanol solution under visible-light irradiation, because of the compositional uniformity and unique surface morphology with large BET surface area of the photocatalyst. The composition of the photocatalyst was optimized at $NaBi_{0.07}Ta_{0.93}O_3$.

4.2.4. *Multi-step reaction*

In our group, aiming to enhance the visible-light-driven photocatalytic activity, ABO_3 with novel micro-/nano-structures were designed and prepared, and successfully applied to visible-light-driven photocatalytic H_2 or O_2 evolution [112,114]. Hexagonal single-crystal nanosheet-based $NaSbO_3$ hierarchical cuboidal microclusters (i.e., HCMCs) with exposed {001} facets were prepared by means of a facile, surfactant-free hydrothermal reaction at 250 °C for 48 h for the first time. Their growth mechanism was investigated by systematically examining the effect of hydrothermal treatment time and temperature on the crystal structures and particle morphologies of products. Furthermore, based on the similar crystal structure (rhombohedral-phase ilmenite) between $NaSbO_3$ and $AgSbO_3$ to facilitate topotactic transformation, hexagonal single-crystal nanosheet-based $AgSbO_3$ hierarchical cuboidal microclusters with exposed {001} facets were prepared by performing an ion exchange of Ag^+ on the sacrificial template of as-prepared hierarchical $NaSbO_3$ precursor at 220 °C for 24 h (see Fig. 7). The as-prepared hierarchical $AgSbO_3$ (i.e., AgSb–HT) showed higher (1.8 times) photocatalytic activity for visible-light-driven O_2 evolution (initial rate, 460 μmol h^{-1} g_{cat}^{-1}) than $AgSbO_3$ formed by performing an ion exchange of Ag^+ on $NaSbO_3$ precursor prepared by a solid-state reaction (i.e., AgSb–SSR—36 h) (see Fig. 8). The unique structure of hierarchical cuboidal microclusters assembled from single-crystal nanosheets with exposed {001} facets simultaneously optimized all three main processes of the photocatalytic reaction (i.e, photon absorption, separation and migration of photogenerated charge carriers, and redox reaction of photogenerated charge carriers), and therefore enhanced the photocatalytic activity [112]. In addition, the sacrificial templates of microtubular (Cr,Ta)-codoped TiO_2 were prepared by solvothermal reaction and calcination post-treatment, and then were successfully transformed to nanocrystal-based microtubular (Cr,Ta)-codoped $SrTiO_3$ by hydrothermal reaction. The as-prepared hierarchical (Cr,Ta)-codoped $SrTiO_3$ also showed higher photocatalytic activity for visible-light-driven H_2 evolution than (Cr,Ta)-codoped $SrTiO_3$ formed by a solid-state reaction [114]. Consequently, the preparation strategy based on design and transformation of sacrificial templates is an effective method to construct special micro-/nano-structures; and the special micro-/nano-structure design is an effective route to enhance photocatalytic performance.

Besides, other preparation strategies (such as polymerized complex method and sol–gel route) were employed to obtain ABO_3 photocatalysts with special micro-/nano-structures (such as $SrTiO_3$ nanocrystals [72], La-doped $NaTaO_3$ nanocrystals [107], $LiNbO_3$ and $NaNbO_3$ nanowires [84,105]) and with enhanced photocatalytic activities.

Based on the above results, it was found that the micro-/nano-structures of ABO_3 photocatalysts could be adjusted by different preparation strategies, aiming to control the

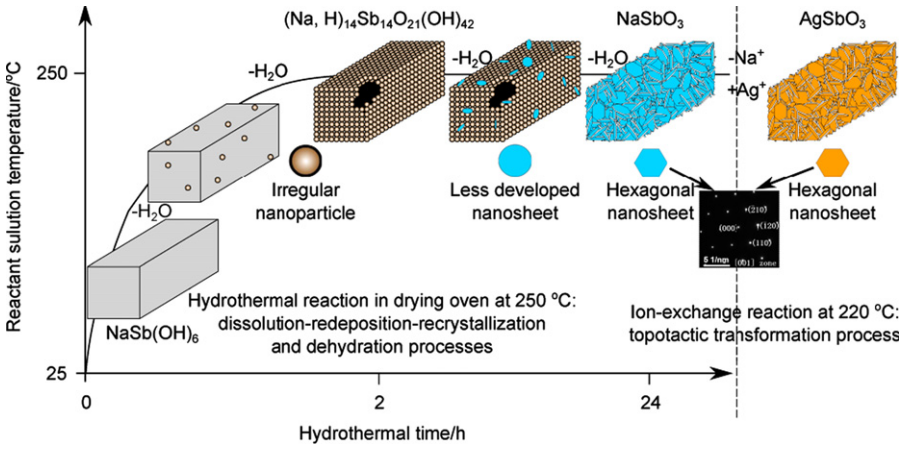

Fig. 7 Schematic illustration of the growth mechanisms of $NaSbO_3$ and $AgSbO_3$ HCMCs during hydrothermal treatment in a drying oven at 250 °C, showing dissolution–redeposition–recrystallization and dehydration processes, followed by an ion-exchange reaction at 220 °C, which results in a topotactic transformation process. Coordinates are nonlinear. Reprinted with permission from Ref. [112].

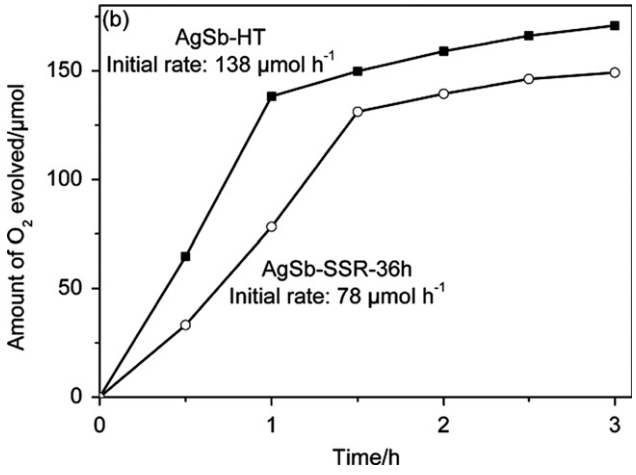

Fig. 8 Time profiles of visible-light-driven O_2 evolution catalyzed by AgSb–SSR—36 h (○; initial rate: 78 μmol h^{-1}) and AgSb–HT (■; initial rate: 138 μmol h^{-1}). Reprinted with permission from Ref. [112].

physicochemical properties, such as crystallinity, crystal size, crystal orientation, surface area, and architecture, and therefore to optimize the whole photocatalytic process.

4.3. Local lattice structure adjustment

Local lattice structure is one of the important physicochemical properties of materials, and hence played a pivotal role in determining the photocatalytic performance. Correspondingly, the local lattice structure adjustment of ABO_3 photocatalysts will be introduced and the structure–activity relationship will be discussed in the following section.

4.3.1. Crystal structures

Crystal structures determined the symmetrical characteristics of crystals, and thus inevitably affected the local lattice structures and photocatalytic performance of materials [30–32,46,53,54,65,67,79].

The relationships between Ta–O–Ta bond angles and photocatalytic activities of ABO_3-based materials were comprehensively investigated by different research groups. Kato et al. prepared a series of alkali tantalate $ATaO_3$ (A = Li, Na, and K) photocatalysts that showed activities for overall water splitting under UV irradiation. The interaction between corner-sharing TaO_6 octahedra in ilmenite $LiTaO_3$ is so weak that the excited energy is localized because of a bond angle of Ta–O–Ta far from 180°. In contrast, the excited energy is delocalized in perovskite $NaTaO_3$ and $KTaO_3$ in which the bond angle are close to 180°. The high activity of NiO/$NaTaO_3$ photocatalyst was in part due to the delocalization of excited energy which were dominated by the slightly distorted connection between TaO_6 octahedra [46]. Teng et al. investigated the effects of crystal structures, especially the Ta–O–Ta bond angles, in $NaTaO_3$ on the photocatalytic activities in detail [30,65,79]. $NaTaO_3$ with monoclinic and orthorhombic phases were prepared by sol–gel and solid-state reaction, respectively. Compared with the orthorhombic $NaTaO_3$, the monoclinic $NaTaO_3$ showed higher photocatalytic activity for H_2 evolution due to the larger surface area and the advantageous features in the electronic and crystal structures. In terms of electronic structure, the monoclinic and orthorhombic phases had indirect and direct bandgaps, respectively. The recombination rate for the photogenerated charge carriers in the monoclinic phase would be much smaller because phonons are involved in the gap transition. In addition, the monoclinic phase was found to have a larger number of effective states available for the photogenerated charge carriers. As for crystal structure, the bond angle of Ta–O–Ta for orthorhombic phase was about 163° while that of the monoclinic phase was close to 180°, which was favorable for delocalization of the excited energy in $NaTaO_3$ [65]. The decrease of photoluminescence intensity with the increase of Ta–O–Ta bond angle directly evidenced that the Ta–O–Ta bond angle affects the separation of photogenerated charge carriers [79]. Furthermore, they improved the photocatalytic activity of $NaTaO_3$ by replacing some Na ions with larger K ions to produce $Na_{1-x}K_xTaO_3$ photocatalysts. K-doping at $x = 0.05$ rectified the distorted perovskite $NaTaO_3$ to a pseudo-cubic phase. The 180° bond angle of Ta–O–Ta in the pseudo-cubic phase may facilitate the separation of photogenerated charges for effective water splitting. Further K-doping (with $x > 0.05$) leads to impurity formation, which bends the Ta–O–Ta linkage and creates

defect states, lowering the photocatalytic activity of $Na_{1-x}K_xTaO_3$ [31].

Besides, the correlation between phonon modes and photocatalytic activities of ABO_3-based $BaM_{1/3}N_{2/3}O_3$ (M = Ni, Zn; N = Nb, Ta) materials were suggested by Yin et al. The Nb-containing photocatalyst in each pair shows higher photocatalytic activity in evolving H_2 from the methanol solution under UV irradiation than the Ta-containing photocatalyst. Raman spectra of these pairs of photocatalysts suggest that some phonon modes in the bending branches for the Ta-containing photocatalyst show an obvious red shift in their frequency, compared with those for the corresponding Nb-containing photocatalyst. Consequently, phonon modes may play an important role in the migration of the photogenerated charge carriers, thus affecting the photocatalytic activity [54].

4.3.2. *Site occupancy*

Owing to the different local lattice environments of A and B sites, as for cations doped ABO_3 photocatalysts, the substitutional sites of doped cations were expected to have important influences on the photocatalytic activities.

Wang et al. prepared two Cr-doped $SrTiO_3$ photocatalysts, $(Sr_{0.95}Cr_{0.05})TiO_3$ with A-site substitution and $Sr(Ti_{0.95}Cr_{0.05})O_3$ with B-site substitution, and found that the H_2 evolution rate over $(Sr_{0.95}Cr_{0.05})TiO_3$ was 100 times more than that over $Sr(Ti_{0.95}Cr_{0.05})O_3$ from aqueous methanol solution under visible-light irradiation. Concerning the charge compensation, the Cr cations located at the Sr^{2+} site were Cr^{3+}, while those doped at the Ti^{4+} site were Cr^{3+} and Cr^{6+}. Cr^{6+} in $Sr(Ti_{0.95}Cr_{0.05})O_3$ behaved as recombination centers of photogenerated charge carriers and therefore reduces the photocatalytic activity. It was thus suggested that the valence states of doped multivalent cations in ABO_3 photocatalysts could be controlled by taking advantages of the charge balance and valence difference at A and B sites [39].

Kanhere et al. prepared a series of Bi-doped $NaTaO_3$ photocatalysts with different substitutional sites for Bi cations. On the one hand, the optical properties of Bi-doped $NaTaO_3$ were tuned by changing the substitutional sites, and Bi ions located at both Na and Ta sites resulted in the narrowest bandgap (2.64 eV). On the other hand, Bi ions at both Na and Ta sites helps maintain the ionic charge balance and thus minimize the native defects (such as oxygen vacancy and cation vacancy). Accordingly, Pt/Bi-doped $NaTaO_3$ with equal A- and B-site substitution was more active than those with either A- or B-site substitution for visible-light-driven H_2 evolution because of the optimized electronic structures for bandgap narrowing to absorb visible-light absorption and the favorable crystal structures for depressing lattice defects to reduce the recombination of photogenerated charge carriers [120].

In our recent work, aiming to mediate the contradiction between the utilization of low-energy photons (visible light) and the preservation of the redox abilities of photogenerated charge carriers and thus to provide a new route to develop single photocatalyst for overall water splitting under visible-light irradiation, upconversion luminescent agent doped ABO_3 were designed and prepared, and successfully applied to visible-light-driven photocatalytic H_2 and O_2 evolution. Furthermore, in order to promote the excitation of photogenerated charge carriers, site-selected doping was adopted to optimize the local lattice environment. A series of upconversion luminescent Er^{3+} doped $SrTiO_3$ photocatalysts with different initial molar ratios of Sr/Ti (i.e., Sr*x*Ti*y*–Er, Sr/Ti = *x*/*y*) have been prepared by a facile polymerized complex method. Er^{3+} ions, which were gradually transferred from the A to the B-site with increasing Sr/Ti, enabled the absorption of visible light by intraband transition and the generation of high-energy excited states by upconversion processes. Compared with those with A-site occupancy, Er^{3+} ions with B-site occupancy are located in distorted BO_6 octahedra with dipole moments and thus subject to much stronger local internal fields, which promotes energy transfer from the high-energy excited states of Er^{3+} to the host $SrTiO_3$ and facilitates the generation of charge carriers in the valence band and conduction band of the host $SrTiO_3$ (see Fig. 9). Consequently, Er-doped $SrTiO_3$ with B-site occupancy instead of A-site occupancy are validated as novel, stable, and efficient photocatalysts for visible-light-driven H_2 (rate, 46.23 μmol h^{-1} g_{cat}^{-1}) and O_2 evolution (initial rate, 44.23 μmol h^{-1} g_{cat}^{-1}) (see Fig. 10). The results generally suggest that the introduction of upconversion luminescent agent into host semiconductor is a promising approach to simultaneously harness low-energy photons and maintain redox ability for photocatalytic H_2 and O_2 evolution and that the local lattice environment of doped element greatly determines the photocatalytic activity [115].

The above results demonstrated that site-selected doping of cations into ABO_3 host is an effective route to improve the photocatalytic performance. However, it was noted that the substitutional sites should be appropriately selected depending

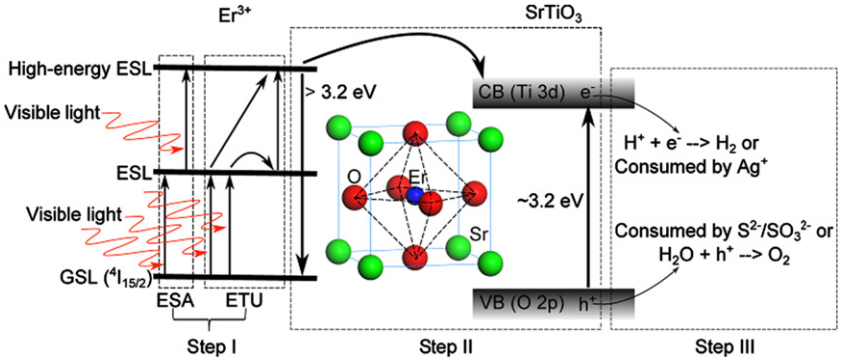

Fig. 9 Schematic illustration of the main processes of the photocatalytic reaction on Sr*x*Ti*y*–Er samples. Step I: Generation of high-energy excited states in Er^{3+} by the absorption of low-energy photons. Step II: Band-to-band excitation of $SrTiO_3$ by energy transferred from high-energy excited states in Er^{3+}. Step III: Redox reactions (see the detailed reaction mechanisms in the Supporting Information). Reprinted with permission from Ref. [115].

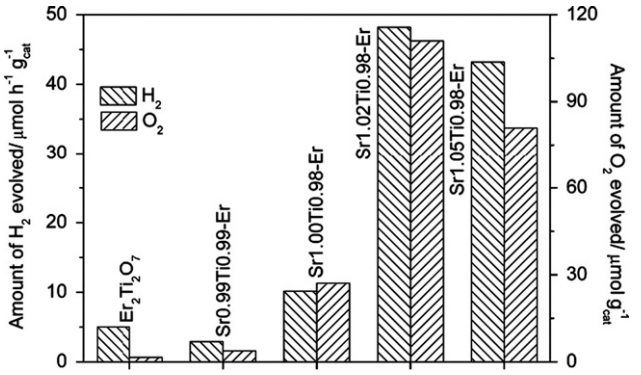

Fig. 10 Visible-light-driven photocatalytic activity for H_2 and O_2 evolution on different samples. The "Amount of O_2 evolved" value corresponds to the amount of O_2 evolved during the first 3 h of the photocatalytic reaction and g_{cat}^{-1} represents "per gram photocatalyst". Reprinted with permission from Ref. [115].

on the specific objectives, such as valence-state control, band-structure adjustment, or energy-transfer enhancement.

The effect of cation ordering in ABO_3-based Sr–Al–Nb–O double perovskite (SAN) on the photocatalytic activity was revealed by Iwakura et al. for the first time. SAN particles had a domain structure of completely B-site ordered (Sr_2AlNbO_6) and disordered ($SrAl_{0.5}Nb_{0.5}O_3$) phases. It was found that photocatalytic activities of SAN for the evolution of H_2 and O_2 respectively from aqueous solutions of methanol and AgF decreased with increasing the fraction of the ordered phase. These results suggested that the photocatalytic activity of ordered Sr_2AlNbO_6 should be lower than that of disordered $SrAl_{0.5}Nb_{0.5}O_3$, although the reason need to be clarified in future studies [89].

Wu et al. investigated the relationship between cation-filling and photocatalytic activity of $AxBO_3$-based tunnel-structure materials for the first time. The catalytic efficiency decreases quasi-linearly with the A-site cation filling of the deficient perovskite A_xNbO_3 (A = K, Na, Sr, Ba) and the ideal perovskite $ATiO_3$ (A = Mg, Ca, Sr, Ba). A lower cation filling in the A-site correlates with higher mobility and improved the separation and transport of photogenerated charge carriers, and therefore resulted in higher photocatalytic activity. Moreover, the linear correlation also holds for the reported tunnel photocatalysts of Bi_2RNbO_7 (R = Y, rare earth element), MIn_2O_4 (M = Ca, Sr, Ba), $ATaO_3$ (A = Li, Na, K), etc. This study not only demonstrates that it is important to take cation filling into account when ranking activity of tunnel-structure photocatalysts, but also discloses some insights for developing new photocatalysts from crystal chemistry [141].

In addition to the control of crystal structures and site occupancy, other strategies such as surface modification were also employed to adjust the local lattice structures of ABO_3-based photocatalysts. Recently, Ouyang et al. successfully improved the activity of photocatalytic H_2 evolution over $SrTiO_3$-based photocatalysts by surface alkalinization. It was found that surface alkalization could significantly shift surface conduction band of $SrTiO_3$ photocatalyst to a more negative level, which supplies a strong potential for H_2O reduction and consequently promote the photocatalytic efficiency of H_2 evolution. This mechanism is also applicable for the visible-light-sensitive (La,Cr)-codoped $SrTiO_3$. Hence this photocatalyst could achieve a high apparent quantum efficiency of 25.6% at around 425 nm for H_2 evolution in methanol aqueous solution containing 5 M NaOH [113].

4.4. *Application of the modification strategy of ABO_3 photocatalysts in designing $A_xB_yO_z$ photocatalysts*

In our recent work, aiming to enhance the visible-light-driven photocatalytic activity and apply the modification strategies of ABO_3 to $A_xB_yO_z$, $A_xB_yO_z$ with continuously adjusted chemical components and micro-/nano-structures were designed and prepared for visible-light-driven photocatalytic H_2 evolution. A series of cubic-phase pyrochlore structure tin(II) antimonate photocatalysts with continuously adjusted chemical components and micro-/nano-structures (i.e., SnSb–T °Cth) were successfully prepared by facile ion-exchange processes with varied ion-exchange time (t) and temperature (T) on the antimonic acid precursor (HSb). With the increase of Sn^{2+} contents in as-prepared tin(II) antimonate photocatalysts, the extended light-response range due to the narrowed bandgaps enhanced the absorption of photons and the excitation of photogenerated charge carriers (see Fig. 11). The micro-/nano-structures were gradually transformed from regular octahedra around 100 nm to nanocrystallines with smaller sizes, and such nanostructural transformation gradually increased the BET surface areas and pore volumes. The decreased crystal sizes shortened the migration distance of photogenerated charge carriers to the reactive sites for redox reactions on the surfaces and thus reduced the recombination of photogenerated charge carriers; the increased BET surface areas enriched the reactive sites, and also enhanced the adsorption of reactants, while the enlarged pore volumes facilitated the accumulation of reactants as well, thereby accelerating the redox reactions. The approaching stoichiometric compositions (molar ratio of Sn/Sb equal to 1) reduced the crystal lattice defects to restrain the recombination of photogenerated charge carriers. Accordingly, the activities of visible-light-driven photocatalytic H_2 evolution were gradually improved and amounted to the highest rate of 40.10 μmol h^{-1} g_{cat}^{-1} for stoichiometric $Sn_2Sb_2O_7$ (see Fig. 12). However, with the further increase of Sn^{2+} content, the activity sharply decreased due to the nonstoichiometric compositions that increased the crystal lattice defects to accelerate the recombination of photogenerated charge carriers, although the bandgaps and micro-/nano-structures seemed to be further optimized (see Fig. 12). As a result, the as-prepared tin(II) antimonates—especially $Sn_2Sb_2O_7$ were validated to be novel, stable photocatalysts for visible-light-driven H_2 evolution. The control of physicochemical properties based on continuous adjustment of chemical components and micro-/nano-structures is an effective approach to optimize all the processes of photocatalytic reaction and finally enhance photocatalytic activity. It is validated to apply the modification strategies of ABO_3 to $A_xB_yO_z$ based on the similarity between ABO_3 and other $A_xB_yO_z$ [142,143].

5. Application of ABO_3 photocatalysts in *Z*-scheme systems for overall water splitting

It is very difficult for a single-photocatalyst system to fulfill the requirements of a narrow bandgap for visible-light absorption

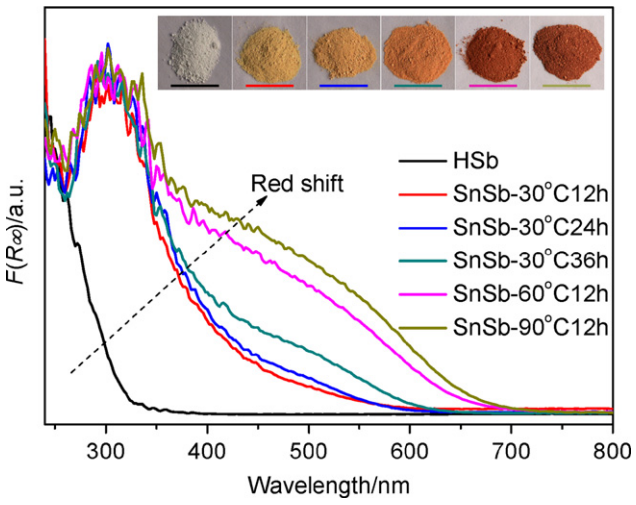

Fig. 11 UV/vis spectra of HSb and SnSb–T °Cth samples. Along the direction of the arrow: HSb, SnSb—30 °C12 h, SnSb—30 °C24 h, SnSb—30 °C36 h, SnSb—60 °C12 h, and SnSb—90 °C12 h. $F(R_\infty)$ was the Kubelka–Munk function. Reprinted with permission from Refs. [142,143].

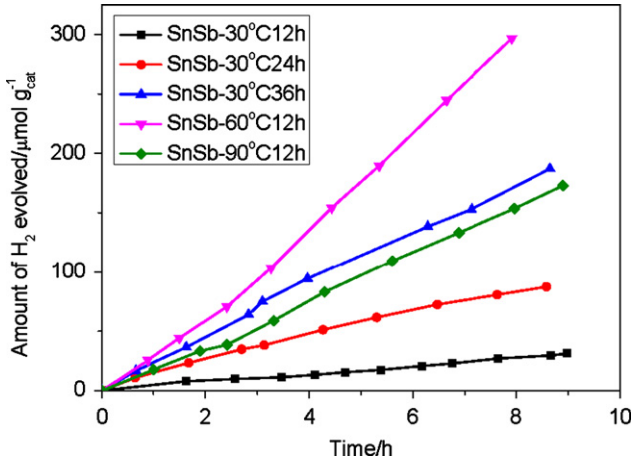

Fig. 12 Time courses of visible-light-driven photocatalytic H_2 evolution on SnSb–T °Cth samples. Reprinted with permission from Refs. [142,143].

and suitable band-edge positions for redox reactions simultaneously. Consequently, single photocatalysts for overall water splitting under visible-light irradiation are rarely reported to date. *Z*-scheme system mimics the photosynthesis process of green plants, and is composed of a photocatalyst for H_2 evolution (i.e., H_2-photocatalyst), a photocatalyst for O_2 evolution (i.e., O_2-photocatalyst), and electron mediator (not indispensable). Based on a two-photon process in the *Z*-scheme system, photocatalysts with solely ability to evolve H_2 or O_2 from the corresponding sacrificial reagents under visible-light irradiation could be coupled effectively, thus realizing visible-light-driven overall water splitting [24].

As discussed above, a variety of ABO_3 structure-based photocatalysts for half-reaction of H_2 or O_2 evolution under visible-light irradiation were developed by means of different modification strategies. Accordingly, ABO_3 photocatalyst-based *Z*-scheme systems could be constructed to realize visible-light-driven overall water splitting (see Table 2). The electron mediators in the *Z*-scheme system play important roles in coupling the two H_2- and O_2-photocatalysts, respectively, and in shuttling the photogenerated carriers. The currently developed Z-scheme systems could be classified as those with ionic electron mediators, with solid electron mediators, and without electron mediators.

5.1. *Z-scheme systems with ionic electron mediators*

Ionic electron mediators in *Z*-scheme systems included IO^{3-}/I^- [99,144,146,150,153], Fe^{3+}/Fe^{2+} [147,149,151], etc. Sayama et al. reported the first *Z*-scheme system (Pt/(Cr,Ta)-codoped $SrTiO_3$|Pt/WO_3) for visible-light-driven overall water splitting by using Pt/(Cr,Ta)-codoped $SrTiO_3$ and Pt/WO_3 as H_2 and O_2-photocatalysts, respectively, and by using IO^{3-}/I^- as electron mediator. The AQY was determined to be ca. 1% at 420 nm [144–146]. Hara and Irie prepared two types of $SrTiO_3$-based photocatalysts, (Bi,Ga)-codoped $SrTiO_3$ and (In,V)-codoped $SrTiO_3$, both of which formed isolated minibands in the forbidden band and thus could absorb visible light. Furthermore, they established a *Z*-scheme system (Pt/(Bi,Ga)-codoped $SrTiO_3$|Pt/(In,V)-codoped $SrTiO_3$) by using the as-prepared $SrTiO_3$-based photocatalysts and IO^{3-}/I^- electron mediator. It was found that visible light contributed to overall water splitting and enhanced the photocatalytic activity [153]. In addition to doped ABO_3 photocatalysts, ABO_3-based solid-solution photocatalysts were employed to construct *Z*-scheme system as well [99,150]. Matoba et al. prepared $BaZrO_3$–$BaTaO_2N$ solid solution, which was coupled with WO_3 to form a *Z*-scheme system (Pt/$BaZrO_3$–$BaTaO_2N$ solid solution/Pt/WO_3) in IO^{3-}/I^- solution. The AQY for overall water splitting was calculated to be about 0.6% at 420–440 nm [99].

In addition to IO^{3-}/I^-, Fe^{3+}/Fe^{2+} was also widely employed to construct *Z*-scheme systems. Sasaki et al. built a *Z*-scheme system consisting of Rh-doped $SrTiO_3$ for H_2 evolution, $BiVO_4$ for O_2 evolution, and Fe^{3+}/Fe^{2+} for an electron mediator, and investigated the effect of cocatalysts loaded on Rh-doped $SrTiO_3$ on photocatalytic reaction. It was found that compared with the system using a Pt cocatalyst (Pt/Rh-doped $SrTiO_3$|$BiVO_4$), the system using a Ru cocatalyst (Ru/Rh-doped $SrTiO_3$|$BiVO_4$) showed comparable activity in the initial stage but exhibited no deactivation process for visible-light-driven overall water splitting. The back-reactions, such as, water formation from H_2 and O_2, reduction of Fe^{3+} by H_2, and oxidation of Fe^{2+} by O_2 were significantly suppressed in the system of Ru/Rh-doped $SrTiO_3$|$BiVO_4$, which gave an AQY of 0.3% [147]. Alternatively, in order to realize the separation of evolved H_2 and O_2 and thus to prevent back-reactions in the *Z*-scheme system of Pt/Rh-doped $SrTiO_3$|$BiVO_4$, Yu et al. designed a twin reactor with a Nafion membrane to divide H_2- and O_2-photocatalysts in two compartments, respectively. It was found that the water-splitting reaction in the twin reactor did not delayed by the membrane through which the electron mediator of Fe^{3+}/Fe^{2+} was diffused, and the deactivation of Pt/Rh-doped $SrTiO_3$ could be minimized due to the suppression of $Fe(OH)_3$ formation on the photocatalyst surface [151].

Table 2 ABO_3-based Z-scheme system for overall water splitting.

H_2-photocatalyst (mass/g)|O_2-photocatalyst (mass/g)	Lamp (filter)[a]	Reactant solution (aqueous)	Activity/$\mu mol \cdot h^{-1} \cdot g_{cat}^{-1}$		AQY/% (wavelength/nm)	Reference (year)
			Cocatalyst/H_2	Cocatalyst/O_2		
(Cr,Ta)-codoped $SrTiO_3$ (0.2)|WO_3 (0.2)	300 W Xe ($\lambda > 420$ nm)	100 mM NaI (pH = =7.0)	0.3 wt% Pt/1.8[b]	1 wt% Pt/0.9[b]	0.1% (420.7)	[141,145] (2001)
(Cr,Ta)-codoped $SrTiO_3$|WO_3	300 W Xe	5 mM NaI	0.3 wt% Pt/16[b]	0.5 wt% Pt/8[b]	1% (420)	[146] (2005)
Rh-doped $SrTiO_3$ (0.05)|$BiVO_4$ (0.05)	300 W Xe ($\lambda > 420$ nm)	2 mM $FeCl_3$+H_2SO_4 (pH = =2.4)	0.7 wt% Ru/~18.5[b]	—/~9[b]	0.3% (420)	[147] (2008)
Rh-doped $SrTiO_3$ (0.1)|$BiVO_4$ (0.1)	300 W Xe ($\lambda > 420$ nm)	H_2SO_4 (pH = =3.5)	1 wt% Ru/40[b]	—/19[b]	1.7% (420)	[148] (2009)
Rh-doped $SrTiO_3$ (0.2)|WO_3 (0.2)	450 W Hg ($\lambda > 420$ nm)	10 mM $FeCl_2$	0.5 wt% Pt/2.7[b]	0.7 wt% Pt/1.1[b]	–	[149] (2009)
$ATaO_2N$ (A = Ca, Sr, Ba) (0.1)|WO_3(0.1)	300 W Xe ($\lambda > 420$ nm)	5 mM NaI	0.3 wt% Pt/~6.4[b]	0.5 wt% Pt/~3.0[b]	0.1% (420–440)	[150] (2009)
$BaZrO_3$–$BaTaO_2N$ (0.05)|WO_3 (0.1)	300 W Xe ($420 < \lambda < 800$ nm)	1 mM NaI	0.3 wt% Pt/~5.5[b]	0.3 wt% Pt/~3[b]	0.6% (420–440)	[99] (2011)
Rh-doped $SrTiO_3$ (0.4)|$BiVO_4$ (0.4)	300 W Xe	5 mM $FeCl_2$+H_2SO_4 (pH = =2.4)|5 mM $FeCl_3$+H_2SO_4 (pH = =2.4)	0.8 wt% Pt/0.84	—/0.41	–	[151] (2011)
Rh-doped $SrTiO_3$ (0.03)|$BiVO_4$ (0.03)	300 W Xe ($\lambda > 420$ nm)	H_2SO_4 (pH = =3.5)	0.7 wt% Ru/11[b]	—/5.5[b]	1.03% (420)	[152] (2011)
$Sr(V_{0.005}Ti_{0.99}In_{0.005})O_3$ (0.03)|$(Bi_{0.1}Sr_{0.9})(Ti_{0.9}Ga_{0.1})O_3$ (0.03)	Xe	0.01 M NaI	0.1 wt% Pt/~0.8	0.1 wt% Pt/~0.3	–	[153] (2012)

[a]The lamp (with filter if necessary) was used as light source.
[b]The rate unit of gas evolution is $\mu mol\ h^{-1}$.

5.2. *Z-scheme systems with solid electron mediators*

Although ionic electron mediators performed efficiently in relaying electrons, a solid electron mediator is more favorable in terms of recovery of the photocatalyst and reclamation of clean water. Tada et al. designed the first all-solid-state *Z*-scheme system of CdS/Au/TiO_2 by using metallic Au as a solid electron mediator [154]. Using photoreduced graphene oxide (PRGO) as solid electron mediator, Iwase et al. coupled the photocatalysts of Rh-doped $SrTiO_3$ ($SrTiO_3$:Rh) for H_2 evolution and $BiVO_4$ for O_2 evolution to construct a novel *Z*-scheme system of Ru/Rh-doped $SrTiO_3$\|$BiVO_4$ [152]. It was demonstrated that PRGO could shuttle photogenerated electrons from $BiVO_4$ to Rh-doped $SrTiO_3$ (see Fig. 13). The PRGO prepared by $BiVO_4$ possesses a high electron conductivity and a low degree of hydrophobicity, thus guaranteeing the efficient electron transfer and tripling the water splitting reaction under visible-light irradiation. An AQY of 1.03% at 420 nm was achieved in the *Z*-scheme system for overall water splitting.

5.3. *Z-scheme systems without electron mediators*

Generally, an electron mediator is required to construct a Z-scheme system. However, the affinity and energy-level matching between photocatalysts and electron mediators actually limit such a combination to several systems. Moreover, the electron mediators may give undesirable effects such as back-reactions to form water from H_2 and O_2 evolved, or their intermediates to shield incident light. In order to exclude the negative effects by electron mediators and to simplify the design, Sasaki et al. fabricated the first *Z*-scheme system (Ru/Rh-doped $SrTiO_3$\|-$BiVO_4$) driven by the interparticle electron transfer between two photocatalysts without an electron mediator for visible-light-driven overall water splitting (see Fig. 14). It was found that the photocatalytic activities were dependent on pH and the highest activity was obtained at pH 3.5, under which the two photocatalysts of Ru/Rh-doped $SrTiO_3$ and $BiVO_4$ were aggregated with suitable contact. Such intimate contact and the Rh species with reversible redox properties in Rh-doped $SrTiO_3$ facilitated the interparticle electron transfer from the conduction band of $BiVO_4$ to impurity level of Rh-doped $SrTiO_3$, and therefore improved the photocatalytic activity. The AQY of the Ru/Rh-doped $SrTiO_3$\|$BiVO_4$ system was 1.7% at 420 nm [148].

The above results announced that the *Z*-scheme system paved an alternative way to visible-light-driven overall water splitting by using ABO_3 structure-based photocatalysts and verified the values of the ABO_3 structure-based photocatalysts that could only evolve H_2 or O_2 in corresponding sacrificial reagents.

6. Summary and perspectives

In summary, major progress on the development of ABO_3-based photocatalysts for water splitting has been achieved by means of different modification strategies based on the fundamental principle and process of photocatalysis and on

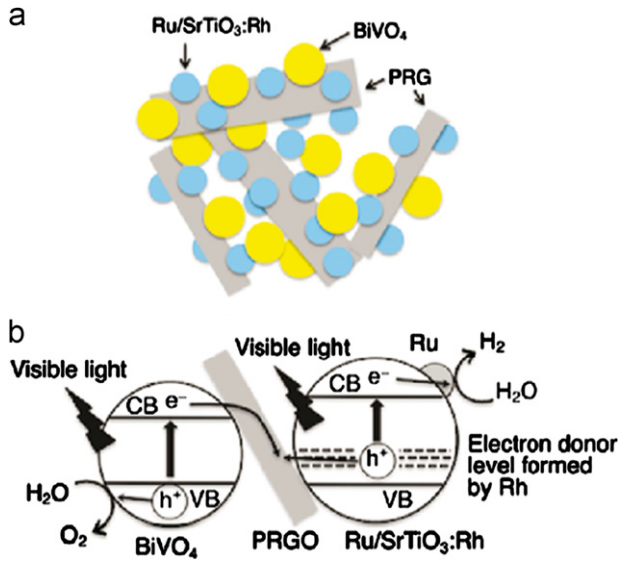

Fig. 13 (a) Schematic image of a suspension of $Ru/SrTiO_3$ and $PRGO/BiVO_4$ in water at pH 3.5. (b) Mechanism of water splitting in a Z-scheme photocatalysis system consisting of $Ru/SrTiO_3$:Rh and $PRGO/BiVO_4$ under visible-light irradiation. Reprinted with permission from Ref. [152].

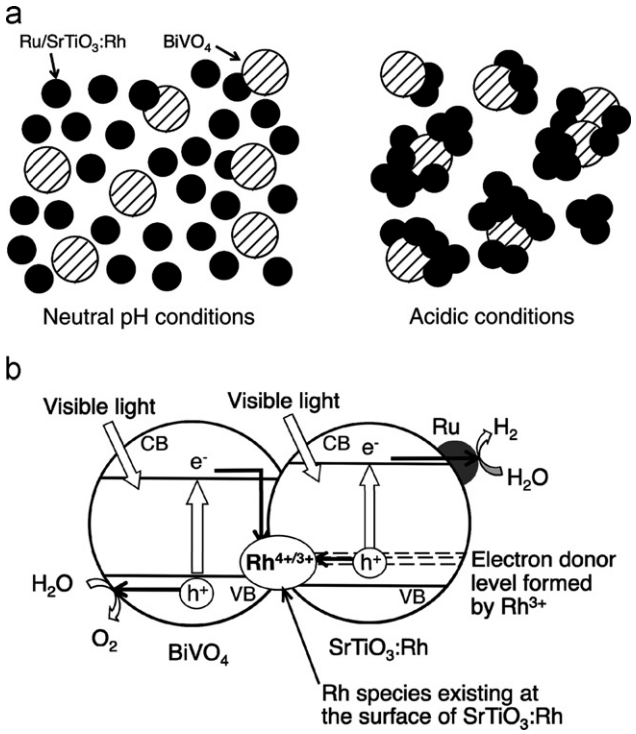

Fig. 14 Mechanism of water splitting using the Z-scheme photocatalysis system driven by electron transfer between H_2- and O_2-photocatalysts. (a) Suspension of $Ru/SrTiO_3$:Rh and $BiVO_4$ at neutral and acidic conditions. (b) Scheme of photocatalytic water splitting. Reprinted with permission from Ref. [148].

the crystal structure and chemical component characteristics of ABO_3 materials. The results demonstrated the encouraging prospects of ABO_3-based photocatalysts and offered a guide for future research work.

ABO_3 photocatalysts with typical crystal structures and chemical components, such as $SrTiO_3$ and $NaTaO_3$, have important research values as model photocatalysts to reveal the structure–activity relationships. Early in 1976, $SrTiO_3$ was proved to be an excellent photocatalyst for overall water splitting under UV irradiation due to its high stability and suitable band-edge positions [155], and, since then, has been extensively investigated by optimizing, for example, the reactant solution [123], cocatalyst [125,126,128,156,157], preparation method [127], and defects [81]. The reported results provided abundant data for future research on photocatalytic mechanism.

Modification of ABO_3 photocatalysts by combining different modification strategies is favorable for optimizing the whole process (i.e., absorption of photons and excitation of the photogenerated charge carriers, separation and migration of the photogenerated charge carriers, and redox reactions) during photocatalytic reaction, and finally improved the photocatalytic performance.

Development of ABO_3-based photocatalysts for overall water splitting under visible-light irradiation remains a great challenge but is still promising if appropriate strategies, such as the incorporation of upconversion luminescent agents (Er, Ho, Eu, Nd, Tm, and so on) and the construction of *Z*-scheme system, is employed. As for Er-doped $SrTiO_3$ [115], both abilities to produce H_2 and O_2 in corresponding sacrificial reagents under visible-light irradiation testified to the fulfilment of thermodynamic conditions for visible-light-driven overall water splitting. Further systematic and detailed work on the improvement of dynamic conditions (such as separation and migration of photogenerated charge carriers, and redox reactions), by optimizing reactant solution and cocatalyst, is in progress in our group in order to realize overall water splitting under visible-light irradiation.

Preparation of ABO_3 film photocatalysts is favorable for photoelectrochemical characterization and performance evaluation so that more physicochemical properties can be obtained for more comprehensive understanding of ABO_3 powder photocatalysts. Furthermore, novel preparation strategies need to be developed due to the challenge of multicomponent metal oxide films.

Acknowledgments

This work was supported by the National Natural Science Foundation of China (NSFC) (Nos. 50821064 and 51121092) and the National Basic Research Program of China (973 Program) (No. 2009CB220000). Jinwen Shi thanks Bing Wang for assisting the literature classification and Table preparation, and the anonymous reviewers for valuable comments and suggestions on an earlier draft of this paper.

References

[1] N.S. Lewis, D.G. Nocera, Powering the planet: chemical challenges in solar energy utilization, Proceedings of the National Academy of Sciences of the United States of America 103 (2006) 15729–15735.

[2] A. Fujishima, K. Honda, Electrochemical photolysis of water at a semiconductor electrode, Nature 238 (1972) 37–38.

[3] Z.G. Zou, J.H. Ye, K. Sayama, H. Arakawa, Direct splitting of water under visible light irradiation with an oxide semiconductor photocatalyst, Nature 414 (2001) 625–627.
[4] K. Maeda, K. Teramura, D.L. Lu, T. Takata, N. Saito, Y. Inoue, K. Domen, Photocatalyst releasing hydrogen from water, Nature (2006) 295.
[5] H.J. Yan, J.H. Yang, G.J. Ma, G.P. Wu, X. Zong, Z.B. Lei, J.Y. Shi, C. Li, Visible-light-driven hydrogen production with extremely high quantum efficiency on Pt–PdS/CdS photocatalyst, Journal Of Catalysis 266 (2009) 165–168.
[6] Z.G. Yi, J.H. Ye, N. Kikugawa, T. Kako, S.X. Ouyang, H. Stuart-Williams, H. Yang, J.Y. Cao, W.J. Luo, Z.S. Li, Y. Liu, R.L. Withers, An orthophosphate semiconductor with photooxidation properties under visible-light irradiation, Nature Materials 9 (2010) 559–564.
[7] X.B. Chen, L. Liu, P.Y. Yu, S.S. Mao, Increasing solar absorption for photocatalysis with black hydrogenated titanium dioxide nanocrystals, Science 331 (2011) 746–750.
[8] A.F. Heyduk, D.G. Nocera, Hydrogen produced from hydrohalic acid solutions by a two-electron mixed-valence photocatalyst, Science 293 (2001) 1639–1641.
[9] P.W. Du, K. Knowles, R. Eisenberg, A homogeneous system for the photogeneration of hydrogen from water based on a platinum(II) terpyridyl acetylide chromophore and a molecular cobalt catalyst, Journal of the American Chemical Society 130 (2008) 12576–12577.
[10] P. Du, J. Schneider, L. Fan, W. Zhao, U. Patel, F.N. Castellano, R. Eisenberg, Bi- and terpyridyl platinum(II) chloro complexes: molecular catalysts for the photogeneration of hydrogen from water or simply precursors for colloidal platinum? Journal of the American Chemical Society 130 (2008) 5056–5058.
[11] Y. Wang, X.C. Wang, M. Antonietti, Polymeric graphitic carbon nitride as a heterogenous organocatalyst: from photochemistry to multipurpose catalysis to sustainable chemistry, Angewandte Chemie-International Edition 51 (2012) 68–89.
[12] Y. Zheng, J. Liu, J. Liang, M. Jaroniec, S.Z. Qiao, Graphitic carbon nitride materials: controllable synthesis and applications in fuel cells and photocatalysis, Energy & Environmental Science 5 (2012) 6717–6731.
[13] X.X. Xu, C. Randorn, P. Efstathiou, J.T.S. Irvine, A red metallic oxide photocatalyst, Nature Materials 11 (2012) 595–598.
[14] X.B. Chen, S.H. Shen, L.J. Guo, S.S. Mao, Semiconductor-based photocatalytic hydrogen generation, Chemical Reviews 110 (2010) 6503–6570.
[15] K. Maeda, Photocatalytic water splitting using semiconductor particles: history and recent developments, Journal of Photochemistry and Photobiology C 12 (2011) 237–268.
[16] S.H. Shen, J.W. Shi, P.H. Guo, L.J. Guo, Visible-light-driven photocatalytic water splitting on nanostructured semiconducting materials, International Journal of Nanotechnology 8 (2011) 523–591.
[17] N. Serpone, A.V. Emeline, Semiconductor photocatalysis—past, present, and future outlook, Journal of Physical Chemistry Letters 3 (2012) 673–677.
[18] F.E. Osterloh, Inorganic materials as catalysts for photochemical splitting of water, Chemistry of Materials 20 (2008) 35–54.
[19] Y. Inoue, Photocatalytic water splitting by RuO_2-loaded metal oxides and nitrides with d^0- and d^{10}-related electronic configurations, Energy & Environmental Science 2 (2009) 364–386.
[20] A. Kudo, Y. Miseki, Heterogeneous photocatalyst materials for water splitting, Chemical Society Reviews 38 (2009) 253–278.
[21] R. Abe, Recent progress on photocatalytic and photoelectrochemical water splitting under visible light irradiation, Journal of Photochemistry and Photobiology C 11 (2010) 179–209.
[22] M. Kitano, M. Hara, Heterogeneous photocatalytic cleavage of water, Journal of Materials Chemistry 20 (2010) 627–641.
[23] K. Maeda, K. Domen, Photocatalytic water splitting: recent progress and future challenges, Journal of Physical Chemistry Letters 1 (2010) 2655–2661.
[24] A. Kudo, Z-scheme photocatalyst systems for water splitting under visible light irradiation, MRS Bulletin 36 (2011) 32–38.
[25] S. Linic, P. Christopher, D.B. Ingram, Plasmonic–metal nanostructures for efficient conversion of solar to chemical energy, Nature Materials 10 (2011) 911–921.
[26] F.E. Osterloh, B.A. Parkinson, Recent developments in solar water-splitting photocatalysis, MRS Bulletin 36 (2011) 17–22.
[27] A. Kubacka, M. Fernandez-Garcia, G. Colon, Advanced nanoarchitectures for solar photocatalytic applications, Chemical Reviews 112 (2012) 1555–1614.
[28] H. Tong, S.X. Ouyang, Y.P. Bi, N. Umezawa, M. Oshikiri, J.H. Ye, Nano-photocatalytic materials: possibilities and challenges, Advanced Materials 24 (2012) 229–251.
[29] U.A. Joshi, A. Palasyuk, D. Arney, P.A. Maggard, Semiconducting oxides to facilitate the conversion of solar energy to chemical fuels, Journal of Physical Chemistry Letters 1 (2010) 2719–2726.
[30] W.H. Lin, C. Cheng, C.C. Hu, H.S. Teng, $NaTaO_3$ photocatalysts of different crystalline structures for water splitting into H_2 and O_2, Applied Physics Letters 89 (2006).
[31] C.C. Hu, Y.L. Lee, H.S. Teng, Efficient water splitting over $Na_{1-x}K_xTaO_3$ photocatalysts with cubic perovskite structure, Journal of Materials Chemistry 21 (2011) 3824–3830.
[32] P. Li, S.X. Ouyang, G.C. Xi, T. Kako, J.H. Ye, The effects of crystal structure and electronic structure on photocatalytic H_2 evolution and CO_2 reduction over two phases of perovskite-structured $NaNbO_3$, Journal of Physical Chemistry C 116 (2012) 7621–7628.
[33] C.H. Li, K.C.K. Soh, P. Wu, Formability of ABO_3 perovskites, Journal of Alloys and Compounds 372 (2004) 40–48.
[34] Z.G. Yi, J.H. Ye, Band gap tuning of $Na_{1-x}La_xTa_{1-x}Co_xO_3$ solid solutions for visible light photocatalysis, Applied Physics Letters 91 (2007) 254108.
[35] D.F. Wang, T. Kako, J.H. Ye, Efficient photocatalytic decomposition of acetaldehyde over a solid-solution perovskite $(Ag_{0.75}Sr_{0.25})(Nb_{0.75}Ti_{0.25})O_3$ under visible-light irradiation, Journal of the American Chemical Society 130 (2008) 2724–2725.
[36] D.F. Wang, T. Kako, J.H. Ye, New series of solid-solution semiconductors $(AgNbO3)_{1-x}(SrTiO_3)_x$ with modulated band structure and enhanced visible-light photocatalytic activity, Journal Of Physical Chemistry C 113 (2009) 3785–3792.
[37] J.J. Ding, J. Bao, S. Sun, Z.L. Luo, C. Gao, Combinatorial discovery of visible-light driven photocatalysts based on the ABO_3-type (A = Y, La, Nd, Sm, Eu, Gd, Dy, Yb, B = Al and In) binary oxides, Journal of Combinatorial chemistry 11 (2009) 523–526.
[38] Z.G. Yi, J.H. Ye, Band gap tuning of $Na_{1-x}La_xTa_{1-x}Cr_xO_3$ for H_2 generation from water under visible light irradiation, Journal of Applied Physics 106 (2009) 074910.
[39] D.F. Wang, J.H. Ye, T. Kako, T. Kimura, Photophysical and photocatalytic properties of $SrTiO_3$ doped with Cr cations on different sites, Journal of Physical Chemistry B 110 (2006) 15824–15830.
[40] Y. Yamada, K. Yano, D.C. Hong, S. Fukuzumi, $LaCoO_3$ acting as an efficient and robust catalyst for photocatalytic water oxidation with persulfate, Physical Chemistry Chemical Physics 14 (2012) 5753–5760.
[41] A. Kudo, I. Mikami, Photocatalytic activities and photophysical properties of $ga_{2-x}in_xo_3$ solid solution, Journal of the Chemical Society—Faraday Transactions 94 (1998) 2929–2932.
[42] T. Ishihara, H. Nishiguchi, K. Fukamachi, Y. Takita, Effects of acceptor doping to $KTaO_3$ on photocatalytic decomposition of pure H_2O, Journal of Physical Chemistry B 103 (1999) 1–3.

[43] A. Kudo, H. Kato, Effect of lanthanide-doping into $NaTaO_3$ photocatalysts for efficient water splitting, Chemical Physics Letters 331 (2000) 373–377.
[44] J. Sato, N. Saito, H. Nishiyama, Y. Inoue, New photocatalyst group for water decomposition of RuO_2-loaded p-block metal (In, Sn, and Sb) oxides with d^{10} configuration, Journal of Physical Chemistry B 105 (2001) 6061–6063.
[45] J. Sato, N. Saito, H. Nishiyama, Y. Inoue, Photocatalytic water decomposition by RuO_2-loaded antimonates, $M_2Sb_2O_7$ (M=Ca, Sr), $CaSb_2O_6$ and $NaSbO_3$, with d^{10} configuration, Journal of Photochemistry and Photobiology A 148 (2002) 85–89.
[46] H. Kato, A. Kudo, Water splitting into H_2 and O_2 on alkali tantalate photocatalysts $ATaO_3$ (A=Li, Na, and K), Journal of Physical Chemistry B 105 (2001) 4285–4292.
[47] H. Kato, A. Kudo, Photocatalytic reduction of nitrate ions over tantalate photocatalysts, Physical Chemistry Chemical Physics 4 (2002) 2833–2838.
[48] H. Kato, H. Kobayashi, A. Kudo, Role of Ag^+ in the band structures and photocatalytic properties of $AgMO_3$ (M: Ta and Nb) with the perovskite structure, Journal of Physical Chemistry B 106 (2002) 12441–12447.
[49] H. Kato, A. Kudo, Visible-light-response and photocatalytic activities of TiO_2 and $SrTiO_3$ photocatalysts codoped with antimony and chromium, Journal Of Physical Chemistry B 106 (2002) 5029–5034.
[50] H. Kato, K. Asakura, A. Kudo, Highly efficient water splitting into H_2 and O_2 over lanthanum-doped $NaTaO_3$ photocatalysts with high crystallinity and surface nanostructure, Journal of the American Chemical Society 125 (2003) 3082–3089.
[51] J. Sato, N. Saito, H. Nishiyama, Y. Inoue, Photocatalytic activity for water decomposition of indates with octahedrally coordinated d^{10} configuration. I. Influences of preparation conditions on activity, Journal of Physical Chemistry B 107 (2003) 7965–7969.
[52] J. Yin, Z.G. Zou, J.H. Ye, Photophysical and photocatalytic properties of $MIn_{0.5}Nb_{0.5}O_3$ (M=Ca, Sr, and Ba), Journal of Physical Chemistry B 107 (2003) 61–65.
[53] J. Yin, Z.G. Zou, J.H. Ye, A novel series of the new visible-light-driven photocatalysts $MCo_{1/3}Nb_{2/3}O_3$ (M=Ca, Sr, and Ba) with special electronic structures, Journal of Physical Chemistry B 107 (2003) 4936–4941.
[54] J. Yin, Z.G. Zou, J.H. Ye, Possible role of lattice dynamics in the photocatalytic activity of $BaM_{1/3}N_{2/3}O_3$ (M=Ni, Zn; N=Nb, Ta), Journal of Physical Chemistry B 108 (2004) 8888–8893.
[55] R. Konta, T. Ishii, H. Kato, A. Kudo, Photocatalytic activities of noble metal ion doped $SrTiO_3$ under visible light irradiation, Journal of Physical Chemistry B 108 (2004) 8992–8995.
[56] T. Ishii, H. Kato, A. Kudo, H_2 evolution from an aqueous methanol solution on $SrTiO_3$ photocatalysts codoped with chromium and tantalum ions under visible light irradiation, Journal of Photochemistry and Photobiology A 163 (2004) 181–186.
[57] J. Yin, Z.G. Zou, J.H. Ye, Photophysical and photocatalytic activities of a novel photocatalyst $BaZn_{1/3}Nb_{2/3}O_3$, Journal of Physical Chemistry B 108 (2004) 12790–12794.
[58] R. Niishiro, H. Kato, A. Kudo, Nickel and either tantalum or niobium-codoped TiO_2 and $SrTiO_3$ photocatalysts with visible-light response for H_2 or O_2 evolution from aqueous solutions, Physical Chemistry Chemical Physics 7 (2005) 2241–2245.
[59] H. Hagiwara, N. Ono, T. Inoue, H. Matsumoto, T. Ishihara, Dye-sensitizer effects on a $Pt/KTa(Zr)O_3$ catalyst for the photocatalytic splitting of water, Angewandte Chemie-International Edition 45 (2006) 1420–1422.
[60] H. Hagiwara, T. Inoue, K. Kaneko, T. Ishihara, Charge-transfer mechanism in $Pt/KTa(Zr)O_3$ photocatalysts modified with porphyrinoids for water splitting, Chemistry—A European Journal 15 (2009) 12862–12870.
[61] J.H. Luo, P.A. Maggard, Hydrothermal synthesis and photocatalytic activities of $SrTiO_3$-coated Fe_2O_3 and $BiFeO_3$, Advanced Materials 18 (2006) 514–517.
[62] J. Yin, Z.G. Zou, J.H. Ye, Sol–gel synthesis and characterization of the photocatalyst $BaCo_{1/3}Nb_{2/3}O_3$, Journal of Materials Science 41 (2006) 1131–1135.
[63] Z.S. Li, T. Yu, Z.G. Zou, J.H. Ye, Degradation in photocatalytic activity induced by hydrogen-related defects in nano-$LiNbO_3$ material, Applied Physics Letters 88 (2006) 071917.
[64] D. Chen, J.H. Ye, $SrSnO_3$ nanostructures: synthesis, characterization, and photocatalytic properties, Chemistry of Materials 19 (2007) 4585–4591.
[65] C.C. Hu, H. Teng, Influence of structural features on the photocatalytic activity of $NaTaO_3$ powders from different synthesis methods, Applied Catalysis A 331 (2007) 44–50.
[66] J.W. Liu, G. Chen, Z.H. Li, Z.G. Zhang, Hydrothermal synthesis and photocatalytic properties of $ATaO_3$ and $ANbO_3$ (A=Na and K), International Journal of Hydrogen Energy 32 (2007) 2269–2272.
[67] Y.P. Yuan, J. Lv, X.J. Jiang, Z.S. Li, T. Yu, Z.G. Zou, J.H. Ye, Large impact of strontium substitution on photocatalytic water splitting activity of $BaSnO_3$, Applied Physics Letters 91 (2007) 094107.
[68] J. Choi, S.Y. Ryu, W. Balcerski, T.K. Lee, M.R. Hoffmann, Photocatalytic production of hydrogen on $Ni/NiO/KNbO_3/CdS$ nanocomposites using visible light, Journal of Materials Chemistry 18 (2008) 2371–2378.
[69] U.A. Joshi, J.S. Jang, P.H. Borse, J.S. Lee, Microwave synthesis of single-crystalline perovskite $BiFeO_3$ nanocubes for photoelectrode and photocatalytic applications, Applied Physics Letters 92 (2008) 242106.
[70] Y.P. Yuan, X.L. Zhang, L.F. Liu, X.J. Jiang, J. Lv, Z.S. Li, Z.G. Zou, Synthesis and photocatalytic characterization of a new photocatalyst $BaZrO_3$, International Journal of Hydrogen Energy 33 (2008) 5941–5946.
[71] B. Zielinska, E. Borowiak-Palen, R.J. Kalenczuk, Photocatalytic hydrogen generation over alkaline-earth titanates in the presence of electron donors, International Journal of Hydrogen Energy 33 (2008) 1797–1802.
[72] Y. Liu, L. Xie, Y. Li, R. Yang, J.L. Qu, Y.Q. Li, X.G. Li, Synthesis and high photocatalytic hydrogen production of $SrTiO_3$ nanoparticles from water splitting under UV irradiation, Journal of Power Sources 183 (2008) 701–707.
[73] S.W. Bae, P.H. Borse, J.S. Lee, Dopant dependent band gap tailoring of hydrothermally prepared cubic $SrTi_xM_{1-x}O_3$ (M=Ru, Rh, ir, Pt, Pd) nanoparticles as visible light photocatalysts, Applied Physics Letters 92 (2008) 104107.
[74] E. Subramanian, J.O. Baeg, S.M. Lee, S.J. Moon, K. Kong, Dissociation of H_2S under visible light irradiation ($\lambda \geq 420$ nm) with $FeGaO_3$ photocatalysts for the production of hydrogen, International Journal of Hydrogen Energy 33 (2008) 6586–6594.
[75] Q.P. Ding, Y.P. Yuan, X. Xiong, R.P. Li, H.B. Huang, Z.S. Li, T. Yu, Z.G. Zou, S.G. Yang, Enhanced photocatalytic water splitting properties of $KNbO_3$ nanowires synthesized through hydrothermal method, Journal of Physical Chemistry C 112 (2008) 18846–18848.
[76] W.J. Luo, Z.S. Li, X.J. Jiang, T. Yu, L.F. Liu, X.Y. Chen, J.H. Ye, Z.G. Zou, Correlation between the band positions of $(SrTiO_3)_{1-x}\bullet(LaTiO_2N)_x$ solid solutions and photocatalytic properties under visible light irradiation, Physical Chemistry Chemical Physics 10 (2008) 6717–6723.
[77] T. Kako, N. Kikugawa, J.H. Ye, Photocatalytic activities of $AgSbO_3$ under visible light irradiation, Catalysis Today 131 (2008) 197–202.
[78] A. Iwase, H. Kato, A. Kudo, The effect of alkaline earth metal ion dopants on photocatalytic water splitting by $NaTaO_3$ powder, ChemSusChem 2 (2009) 873–877.
[79] C.C. Hu, C.C. Tsai, H. Teng, Structure characterization and tuning of perovskite-like $NaTaO_3$ for applications in photoluminescence and photocatalysis, Journal of the American Ceramic Society 92 (2009) 460–466.

[80] G.Q. Li, S.C. Yan, Z.Q. Wang, X.Y. Wang, Z.S. Li, J.H. Ye, Z.G. Zou, Synthesis and visible light photocatalytic property of polyhedron-shaped $AgNbO_3$, Dalton Transactions (2009) 8519–8524.

[81] T. Takata, K. Domen, Defect engineering of photocatalysts by doping of aliovalent metal cations for efficient water splitting, Journal of Physical Chemistry C 113 (2009) 19386–19388.

[82] M. Maruyama, A. Iwase, H. Kato, A. Kudo, H. Onishi, Time-resolved infrared absorption study of $NaTaO_3$ photocatalysts doped with alkali earth metals, Journal of Physical Chemistry C 113 (2009) 13918–13923.

[83] Z.G. Li, Y.X. Wang, J.W. Liu, G. Chen, Y.X. Li, C. Zhou, Photocatalytic hydrogen production from aqueous methanol solutions under visible light over $Na(Bi_xTa_{1-x})O_3$ solid-solution, International Journal of Hydrogen Energy 34 (2009) 147–152.

[84] K. Saito, A. Kudo, Niobium-complex-based syntheses of sodium niobate nanowires possessing superior photocatalytic properties, Inorganic Chemistry 49 (2010) 2017–2019.

[85] Y.P. Yuan, Z.Y. Zhao, J. Zheng, M. Yang, L.G. Qiu, Z.S. Li, Z.G. Zou, Polymerizable complex synthesis of $BaZr_{1-x}Sn_xO_3$ photocatalysts: role of Sn^{4+} in the band structure and their photocatalytic water splitting activities, Journal of Materials Chemistry 20 (2010) 6772–6779.

[86] K. Shimura, H. Yoshida, Hydrogen production from water and methane over Pt-loaded calcium titanate photocatalyst, Energy & Environmental Science 3 (2010) 615–617.

[87] J. Ng, S.P. Xu, X.W. Zhang, H.Y. Yang, D.D. Sun, Hybridized nanowires and cubes: a novel architecture of a heterojunctioned $TiO_2/SrTiO_3$ thin film for efficient water splitting, Advanced Functional Materials 20 (2010) 4287–4294.

[88] C.C. Hu, H.S. Teng, Structural features of p-type semiconducting NiO as a co-catalyst for photocatalytic water splitting, Journal of Catalysis 272 (2010) 1–8.

[89] H. Iwakura, H. Einaga, Y. Teraoka, Relationship between cation arrangement and photocatalytic activity for Sr–Al–Nb–O double perovskite, Inorganic Chemistry 49 (2010) 11362–11369.

[90] H.J. Zhang, G. Chen, Y.X. Li, Y.J. Teng, Electronic structure and photocatalytic properties of copper-doped $CaTiO_3$, International Journal of Hydrogen Energy 35 (2010) 2713–2716.

[91] J.J. Li, L.S. Jia, W.P. Fang, J.L. Zeng, Enhancement of activity of $LaNi_{0.7}Cu_{0.3}O_3$ for photocatalytic water splitting by reduction treatment at moderate temperature, International Journal of Hydrogen Energy 35 (2010) 5270–5275.

[92] T. Puangpetch, P. Sommakettarin, S. Chavadej, T. Sreethawong, Hydrogen production from water splitting over eosin Y-sensitized mesoporous-assembled perovskite titanate nanocrystal photocatalysts under visible light irradiation, International Journal of Hydrogen Energy 35 (2010) 12428–12442.

[93] T. Puangpetch, T. Sreethawong, S. Chavadej, Hydrogen production over metal-loaded mesoporous-assembled $SrTiO_3$ nanocrystal photocatalysts: effects of metal type and loading, International Journal of Hydrogen Energy 35 (2010) 6531–6540.

[94] J.J. Li, J.L. Zeng, L.S. Jia, W.P. Fang, Investigations on the effect of Cu^{2+}/Cu^{1+} redox couples and oxygen vacancies on photocatalytic activity of treated $LaNi_{1-x}Cu_xO_3$ ($x=0.1$, 0.4, 0.5), International Journal of Hydrogen Energy 35 (2010) 12733–12740.

[95] K. Shimura, S. Kato, T. Yoshida, H. Itoh, T. Hattori, H. Yoshida, Photocatalytic steam reforming of methane over sodium tantalate, Journal of Physical Chemistry C 114 (2010) 3493–3503.

[96] J. Lv, T. Kako, Z.S. Li, Z.G. Zou, J.H. Ye, Synthesis and photocatalytic activities of $NaNbO_3$ rods modified by In_2O_3 nanoparticles, Journal of Physical Chemistry C 114 (2010) 6157–6162.

[97] S. Boumaza, A. Boudjemaa, A. Bouguelia, R. Bouarab, M. Trari, Visible light induced hydrogen evolution on new heterosystem $ZnFe_2O_4/SrTiO_3$, Applied Energy 87 (2010) 2230–2236.

[98] K.M. Parida, K.H. Reddy, S. Martha, D.P. Das, N. Biswal, Fabrication of nanocrystalline $LaFeO_3$: an efficient sol–gel auto-combustion assisted visible light responsive photocatalyst for water decomposition, International Journal of Hydrogen Energy 35 (2010) 12161–12168.

[99] T. Matoba, K. Maeda, K. Domen, Activation of $BaTaO_2N$ photocatalyst for enhanced non-sacrificial hydrogen evolution from water under visible light by forming a solid solution with $BaZrO_3$, Chemistry—A European Journal 17 (2011) 14731–14735.

[100] J.X. Sun, G. Chen, Y.X. Li, R.C. Jin, Q. Wang, J. Pei, Novel $(Na,K)TaO_3$ single crystal nanocubes: molten salt synthesis, invariable energy level doping and excellent photocatalytic performance, Energy & Environmental Science 4 (2011) 4052–4060.

[101] J.W. Shi, J.H. Ye, Z.H. Zhou, M.T. Li, L.J. Guo, Hydrothermal synthesis of $Na_{0.5}La_{0.5}TiO_3$–$LaCrO_3$ solid-solution single-crystal nanocubes for visible-light-driven photocatalytic H_2 evolution, Chemistry—A European Journal 17 (2011) 7858–7867.

[102] H. Yu, S.X. Ouyang, S.C. Yan, Z.S. Li, T. Yu, Z.G. Zou, Sol–gel hydrothermal synthesis of visible-light-driven Cr-doped $SrTiO_3$ for efficient hydrogen production, Journal of Materials Chemistry 21 (2011) 11347–11351.

[103] H. Husin, W.N. Su, H.M. Chen, C.J. Pan, S.H. Chang, J. Rick, W.T. Chuang, H.S. Sheu, B.J. Hwang, Photocatalytic hydrogen production on nickel-loaded $La_xNa_{1-x}TaO_3$ prepared by hydrogen peroxide-water based process, Green Chemistry 13 (2011) 1745–1754.

[104] T. Yokoi, J. Sakuma, K. Maeda, K. Domen, T. Tatsumi, J.N. Kondo, Preparation of a colloidal array of $NaTaO_3$ nanoparticles via a confined space synthesis route and its photocatalytic application, Physical Chemistry Chemical Physics 13 (2011) 2563–2570.

[105] K. Saito, K. Koga, A. Kudo, Lithium niobate nanowires for photocatalytic water splitting, Dalton Transactions 40 (2011) 3909–3913.

[106] K. Saito, K. Koga, A. Kudo, Molten salt treatment of sodium niobate nanowires affording valence band-controlled $(AgNbO_3)$–$(NaNbO_3)$ nanowires, Nanoscience and Nanotechnology Letters 3 (2011) 686–689.

[107] H. Husin, H.M. Chen, W.N. Su, C.J. Pan, W.T. Chuang, H.S. Sheu, B.J. Hwang, Green fabrication of La-doped $NaTaO_3$ via H_2O_2 assisted sol–gel route for photocatalytic hydrogen production, Applied Catalysis B 102 (2011) 343–351.

[108] X.X. Xu, G. Liu, C. Randorn, J.T.S. Irvine, g-C_3N_4 coated $SrTiO_3$ as an efficient photocatalyst for H_2 production in aqueous solution under visible light irradiation, International Journal of Hydrogen Energy 36 (2011) 13501–13507.

[109] H.W. Kang, S.B. Park, H_2 evolution under visible light irradiation from aqueous methanol solution on $SrTiO_3$:Cr/Ta prepared by spray pyrolysis from polymeric precursor, International Journal of Hydrogen Energy 36 (2011) 9496–9504.

[110] J.W. Liu, Y. Sun, Z.H. Li, S.Y. Li, J.X. Zhao, Photocatalytic hydrogen production from water/methanol solutions over highly ordered Ag–$SrTiO_3$ nanotube arrays, International Journal of Hydrogen Energy 36 (2011) 5811–5816.

[111] P. Dhanasekaran, N.M. Gupta, Factors affecting the production of H_2 by water splitting over a novel visible-light-driven photocatalyst $GaFeO_3$, International Journal of Hydrogen Energy 37 (2012) 4897–4907.

[112] J.W. Shi, J.H. Ye, Q.Y. Li, Z.H. Zhou, H. Tong, G.C. Xi, L.J. Guo, Single-crystal nanosheet-based hierarchical $AgSbO_3$ with exposed {001} facets: topotactic synthesis and enhanced photocatalytic activity, Chemistry—A European Journal 18 (2012) 3157–3162.

[113] S.X. Ouyang, H. Tong, N. Umezawa, J.Y. Cao, P. Li, Y.P. Bi, Y.J. Zhang, J.H. Ye, Surface-alkalinization-induced enhancement of photocatalytic H_2 evolution over $SrTiO_3$-based photocatalysts, Journal of the American Chemical Society 134 (2012) 1974–1977.

[114] J.W. Shi, S.H. Shen, Y.B. Chen, L.J. Guo, S.S. Mao, Visible light-driven photocatalysis of doped $SrTiO_3$ tubular structure, Optics Express 20 (2012) A351–A359.

[115] J.W. Shi, J.H. Ye, L.J. Ma, S.X. Ouyang, D.W. Jing, L.J. Guo, Site-selected doping of upconversion luminescent Er^{3+} into $SrTiO_3$ for visible-light-driven photocatalytic H_2 or O_2 evolution, Chemistry—A European Journal 18 (2012) 7543–7551.

[116] P. Wu, J.W. Shi, Z.H. Zhou, W.D. Tang, L.J. Guo, $CaTaO_2N$–$CaZrO_3$ solid solution: band-structure engineering and visible-light-driven photocatalytic hydrogen production, International Journal of Hydrogen Energy 37 (2012) 13704–13710.

[117] H.W. Kang, S.N. Lim, S.B. Park, Co-doping schemes to enhance H_2 evolution under visible light irradiation over $SrTiO_3$:Ni/M (M=La or Ta) prepared by spray pyrolysis, International Journal of Hydrogen Energy 37 (2012) 5540–5549.

[118] H.W. Kong, S.N. Lim, S.B. Park, Photocatalytic H_2 evolution under visible light from aqueous methanol solution on $NaBi_xTa_{1-x}O_3$ prepared by spray pyrolysis, International Journal of Hydrogen Energy 37 (2012) 4026–4035.

[119] L. Wang, W.Z. Wang, Photocatalytic hydrogen production from aqueous solutions over novel $Bi_{0.5}Na_{0.5}TiO_3$ microspheres, International Journal of Hydrogen Energy 37 (2012) 3041–3047.

[120] P. Kanhere, J.W. Zheng, Z. Chen, Visible light driven photocatalytic hydrogen evolution and photophysical properties of Bi^{3+} doped $NaTaO_3$, International Journal of Hydrogen Energy 37 (2012) 4889–4896.

[121] H.W. Bai, J. Juay, Z.Y. Liu, X.X. Song, S.S. Lee, D.D. Sun, Hierarchical $SrTiO_3/TiO_2$ nanofibers heterostructures with high efficiency in photocatalytic H_2 generation, Applied Catalysis B 125 (2012) 367–374.

[122] K. Domen, S. Naito, M. Soma, T. Onishi, K. Tamaru, Photocatalytic decomposition of water vapour on an NiO–$SrTiO_3$ catalyst, Journal of Chemical Society: Chemical Communications (1980) 543–544.

[123] F.T. Wagner, G.A. Somorjai, Photocatalytic hydrogen-production from water on Pt-free $SrTiO_3$ in alkali hydroxide solutions, Nature 285 (1980) 559–560.

[124] K. Domen, S. Naito, T. Onishi, K. Tamaru, Study of the photocatalytic decomposition of water vapor over a NiO–$SrTiO_3$ catalyst, Journal of Physical Chemistry 86 (1982) 3657–3661.

[125] K. Domen, A. Kudo, T. Onishi, Mechanism of photocatalytic decomposition of water into H_2 and O_2 over NiO–$SrTiO_3$, Journal of Catalysis 102 (1986) 92–98.

[126] K. Domen, A. Kudo, T. Onishi, N. Kosugi, H. Kuroda, Photocatalytic decomposition of water into hydrogen and oxygen over NiO–$SrTiO_3$ powder. 1. Structure of the catalysts, Journal of Physical Chemistry 90 (1986) 292–295.

[127] A. Kudo, A. Tanaka, K. Domen, T. Onishi, The effects of the calcination temperature of $SrTiO_3$ powder on photocatalytic activities, Journal of Catalysis 111 (1988) 296–301.

[128] S. Ikeda, K. Hirao, S. Ishino, M. Matsumura, B. Ohtani, Preparation of platinized strontium titanate covered with hollow silica and its activity for overall water splitting in a novel phase-boundary photocatalytic system, Catalysis Today 117 (2006) 343–349.

[129] X.J. Liu, Z.J. Wu, X.F. Hao, H.P. Xiang, J. Meng, First-principles comparative study of the pressure-induced phase transition of $NaSbO_3$ and $NaBiO_3$, Chemical Physics Letters 416 (2005) 7–13.

[130] M.A. Pena, J.L.G. Fierro, Chemical structures and performance of perovskite oxides, Chemical Reviews 101 (2001) 1981–2017.

[131] J. Brous, I. Fankuchen, E. Banks, Rare earth titanates with a perovskite structure, Acta Crystallographica 6 (1953) 67–70.

[132] A. Wold, R. Ward, Perowskite-type oxides of cobalt, chromium and vanadium with some rare earth elements, Journal of the American Chemical Society 76 (1954) 1029–1030.

[133] K.P. Ong, P. Blaha, P. Wu, Origin of the light green color and electronic ground state of $LaCrO_3$, Physical Review B 77 (2008) 073102.

[134] P.V. Kamat, Manipulation of charge transfer across semiconductor interface. A criterion that cannot be ignored in photocatalyst design, Journal of Physical Chemistry Letters 3 (2012) 663–672.

[135] P.D. Tran, L.H. Wong, J. Barber, J.S.C. Loo, Recent advances in hybrid photocatalysts for solar fuel production, Energy & Environmental Science 5 (2012) 5902–5918.

[136] K. Domen, A. Kudo, T. Onishi, N. Kosugi, H. Kuroda, Photocatalytic decomposition of water into H_2 and O_2 over NiO–$SrTiO_3$ powder. 1. Structure of the catalyst, Journal of Physical Chemistry 90 (1986) 292–295.

[137] J. Baxter, Z.X. Bian, G. Chen, D. Danielson, M.S. Dresselhaus, A.G. Fedorov, T.S. Fisher, C.W. Jones, E. Maginn, U. Kortshagen, A. Manthiram, A. Nozik, D.R. Rolison, T. Sands, L. Shi, D. Sholl, Y.Y. Wu, Nanoscale design to enable the revolution in renewable energy, Energy & Environmental Science 2 (2009) 559–588.

[138] M. Batzill, Fundamental aspects of surface engineering of transition metal oxide photocatalysts, Energy & Environmental Science 4 (2011) 3275–3286.

[139] H.L. Zhou, Y.Q. Qu, T. Zeid, X.F. Duan, Towards highly efficient photocatalysts using semiconductor nanoarchitectures, Energy & Environmental Science 5 (2012) 6732–6743.

[140] K. Byrappa, M. Yoshimura, Handbook of Hydrothermal Technology—A Technology for Crystal Growth and Materials Processing, first ed. William Andrew Publishing, New York, 2001.

[141] J.J. Wu, F.Q. Huang, Z.C. Shan, Y.M. Wang, Quasi-linear dependence of cation filling on the photocatalysis of A_xBO_3-based tunnel compounds, Dalton Transactions 40 (2011) 6906–6911.

[142] J.W. Shi, L.J. Ma, P. Wu, Z.H. Zhou, P.H. Guo, S.H. Shen, D.W. Jing, L.J. Guo, A novel $Sn_2Sb_2O_7$ nanophotocatalyst for visible-light-driven H_2 evolution, Nano Research 5 (2012) 576–583.

[143] J.W. Shi, L.J. Ma, P. Wu, Z.H. Zhou, J.G. Jiang, X.K. Wan, D.W. Jing, L.J. Guo, Tin(II) antimonates with adjustable compositions: effects of bandgaps and nanostructures on visible-light-driven photocatalytic H_2 evolution, ChemCatChem 4 (2012) 1389–1396.

[144] K. Sayama, K. Mukasa, R. Abe, Y. Abe, H. Arakawa, Stoichiometric water splitting into H_2 and O_2 using a mixture of two different photocatalysts and an IO_3^-/I^- shuttle redox mediator under visible light irradiation, Chemical Communications (2001) 2416–2417.

[145] K. Sayama, K. Mukasa, R. Abe, Y. Abe, H. Arakawa, A new photocatalytic water splitting system under visible light irradiation mimicking a Z-scheme mechanism in photosynthesis, Journal of Photochemistry and Photobiology A 148 (2002) 71–77.

[146] R. Abe, K. Sayama, H. Sugihara, Development of new photocatalytic water splitting into H_2 and O_2 using two different semiconductor photocatalysts and a shuttle redox mediator IO_3^-/I^-, Journal of Physical Chemistry B 109 (2005) 16052–16061.

[147] Y. Sasaki, A. Iwase, H. Kato, A. Kudo, The effect of co-catalyst for Z-scheme photocatalysis systems with an Fe^{3+}/Fe^{2+} electron mediator on overall water splitting under visible light irradiation, Journal of Catalysis 259 (2008) 133–137.

[148] Y. Sasaki, H. Nemoto, K. Saito, A. Kudo, Solar water splitting using powdered photocatalysts driven by Z-schematic interparticle electron transfer without an electron mediator, Journal of Physical Chemistry C 113 (2009) 17536–17542.

[149] S.W. Bae, S.M. Ji, S.J. Hong, J.W. Jang, J.S. Lee, Photocatalytic overall water splitting with dual-bed system under visible light irradiation, International Journal of Hydrogen Energy 34 (2009) 3243–3249.
[150] M. Higashi, R. Abe, T. Takata, K. Domen, Photocatalytic overall water splitting under visible light using $ATaO_2N$ (A = Ca, Sr, Ba) and WO_3 in a IO_3^-/I^- shuttle redox mediated system, Chemistry of Materials 21 (2009) 1543–1549.
[151] S.C. Yu, C.W. Huang, C.H. Liao, J.C.S. Wu, S.T. Chang, K.H. Chen, A novel membrane reactor for separating hydrogen and oxygen in photocatalytic water splitting, Journal Of Membrane Science 382 (2011) 291–299.
[152] A. Iwase, Y.H. Ng, Y. Ishiguro, A. Kudo, R. Amal, Reduced graphene oxide as a solid-state electron mediator in Z-scheme photocatalytic water splitting under visible light, Journal of the American Chemical Society 133 (2011) 11054–11057.
[153] S. Hara, H. Irie, Band structure controls of $SrTiO_3$ towards two-step overall water splitting, Applied Catalysis B 115 (2012) 330–335.
[154] H. Tada, T. Mitsui, T. Kiyonaga, T. Akita, K. Tanaka, All-solid-state Z-scheme in CdS–Au–TiO_2 three-component nanojunction system, Nature Materials 5 (2006) 782–786.
[155] M.S. Wrighton, A.B. Ellis, P.T. Wolczanski, D.L. Morse, H.B. Abrahamson, D.S. Ginley, Strontium titanate photoelectrodes. Efficient photoassisted electrolysis of water at zero applied potential, Journal of the American Chemical Society 98 (1976) 2774–2779.
[156] K. Domen, S. Naito, M. Soma, T. Onishi, K. Tamaru, Photocatalytic decomposition of water-vapour on an NiO–$SrTiO_3$ catalyst, Journal of Chemical Society: Chemical Communications (1980) 543–544.
[157] K. Domen, S. Naito, T. Onishi, K. Tamaru, Study of the photocatalytic decomposition of water-vapor over a NiO–$SrTiO_3$ catalyst, Journal of Physical Chemistry 86 (1982) 3657–3661.

Prof. Dr. Liejin Guo is the director of the State Key Laboratory of Multiphase Flow in Power Engineering in Xi'an Jiaotong University, China. He obtained his PhD Degree in Power Engineering and Engineering Thermophysics from Xi'an Jiaotong University in 1989. His research interest includes multiphase flow, heat and mass transfer, and renewable energy technologies. He serves in the editorial boards of several international journals such as International Journal of Hydrogen Energy, International Journal of multiphase flow and Applied Thermal Engineering. He has published more than 400 papers in journals and conferences, given over 30 invited or keynote lectures in international conferences. He has been awarded with the Second Class Prize of National Natural Science Award in 2007 and the Second Class Prize of National Technology Innovation Award in 2009.